AEDC-TR-74-36

DOC_NUM SER CN
UNC22516-PDC A 1

NITROGEN CONDENSATION IN A SONIC ORIFICE EXPANSION FLOW

J. W. L. Lewis, W. D. Williams, L. L. Price,
and H. M. Powell
ARO, Inc.

VON KÁRMÁN GAS DYNAMICS FACILITY
ARNOLD ENGINEERING DEVELOPMENT CENTER
AIR FORCE SYSTEMS COMMAND
ARNOLD AIR FORCE STATION, TENNESSEE 37389

July 1974

Final Report for Period November 1, 1972 – July 31, 1973

Approved for public release; distribution unlimited.

Prepared for

ARNOLD ENGINEERING DEVELOPMENT CENTER (DYFS)
ARNOLD AIR FORCE STATION, TN 37389

NOTICES

When U. S. Government drawings specifications, or other data are used for any purpose other than a definitely related Government procurement operation, the Government thereby incurs no responsibility nor any obligation whatsoever, and the fact that the Government may have formulated, furnished, or in any way supplied the said drawings, specifications, or other data, is not to be regarded by implication or otherwise, or in any manner licensing the holder or any other person or corporation, or conveying any rights or permission to manufacture, use, or sell any patented invention that may in any way be related thereto.

Qualified users may obtain copies of this report from the Defense Documentation Center.

References to named commercial products in this report are not to be considered in any sense as an endorsement of the product by the United States Air Force or the Government.

APPROVAL STATEMENT

This technical report has been reviewed and is approved.

Eules L. Hively

EULES L. HIVELY
Research and Development Division
Directorate of Technology

Robert O Dietz

ROBERT O. DIETZ
Director of Technology

UNCLASSIFIED

SECURITY CLASSIFICATION OF THIS PAGE (When Data Entered)

REPORT DOCUMENTATION PAGE		READ INSTRUCTIONS BEFORE COMPLETING FORM
1. REPORT NUMBER AEDC-TR-74-36	2. GOVT ACCESSION NO.	3. RECIPIENT'S CATALOG NUMBER
4. TITLE (and Subtitle) NITROGEN CONDENSATION IN A SONIC ORIFICE EXPANSION FLOW		5. TYPE OF REPORT & PERIOD COVERED Final Report – November 1, 1972–July 31, 1973
		6. PERFORMING ORG. REPORT NUMBER
7. AUTHOR(s) J. W. L. Lewis, W. D. Williams, L. L. Price, and H. M. Powell, ARO, Inc.		8. CONTRACT OR GRANT NUMBER(s)
9. PERFORMING ORGANIZATION NAME AND ADDRESS Arnold Engineering Development Center Arnold Air Force Station, Tennessee 37389		10. PROGRAM ELEMENT, PROJECT, TASK AREA & WORK UNIT NUMBERS Program Element 65802F
11. CONTROLLING OFFICE NAME AND ADDRESS Arnold Engineering Development Center (DYFS), Arnold AF Station, TN 37389		12. REPORT DATE July 1974
		13. NUMBER OF PAGES 44
14. MONITORING AGENCY NAME & ADDRESS(if different from Controlling Office)		15. SECURITY CLASS. (of this report) UNCLASSIFIED
		15a. DECLASSIFICATION/DOWNGRADING SCHEDULE N/A

16. DISTRIBUTION STATEMENT (of this Report)

Approved for public release; distribution unlimited.

17. DISTRIBUTION STATEMENT (of the abstract entered in Block 20, if different from Report)

18. SUPPLEMENTARY NOTES

Available in DDC.

19. KEY WORDS (Continue on reverse side if necessary and identify by block number)

nitrogen	Rayleigh scattering
condensation	electron beam
orifice flow	fluorescence
expansion	measurement

20. ABSTRACT (Continue on reverse side if necessary and identify by block number)

Homogeneous condensation of nitrogen in hypersonic expansions from a sonic orifice source was investigated using both Rayleigh scattering and electron beam fluorescence diagnostics. Using a 3-mm orifice, the source pressure range of 100 to 4000 torr was investigated for a 300 K source temperature. Electron beam measurements of the rotational temperature, T_R, of nitrogen (N_2) were used to determine onset of condensation, and both radial and axial

DD FORM 1 JAN 73 1473 EDITION OF 1 NOV 65 IS OBSOLETE

UNCLASSIFIED

SECURITY CLASSIFICATION OF THIS PAGE (When Data Entered)

20. Continued.

surveys of T_R were performed. Similar electron beam measurements were performed for source temperatures of 116 K and 133 K for one pressure value. Rayleigh scattering measurements were used to observe both onset of condensation and growth of clusters along the centerline, and estimates of mole or mass fractions of condensate were obtained using both diagnostic techniques. Previously published supersaturation ratios of N_2 determined by other investigators were significantly larger than the present results which observed onset earlier in the flow field.

PREFACE

The work reported herein was conducted at the Arnold Engineering Development Center (AEDC), Air Force Systems Command (AFSC), under the sponsorship of Air Force Cambridge Research Laboratories (AFCRL), AFSC. The AFCRL project monitor was R. E. Good, who provided the technical objectives of the project. The results were obtained by ARO, Inc. (a subsidiary of Sverdrup & Parcel and Associates, Inc.), contract operator of AEDC, AFSC, Arnold Air Force Station, Tennessee. This work was conducted under ARO Project No. VF233, and the manuscript (ARO Control No. ARO-VKF-TR-74-12) was submitted for publication on January 18, 1974.

CONTENTS

	Page
1.0 INTRODUCTION AND THEORY	
1.1 Background and Previous Measurements	5
1.2 Electron Beam Fluorescence Technique	6
1.3 Rayleigh Scattering	7
2.0 EXPERIMENTAL APPARATUS AND METHOD	
2.1 Gas Source and Vacuum Chamber	11
2.2 Electron Beam Apparatus	11
2.3 Rayleigh Scattering Apparatus	17
3.0 RESULTS AND DISCUSSION	
3.1 Rotational Temperature Results	22
3.2 Rayleigh Scattering Results	28
3.3 Analysis and Discussion	34
4.0 CONCLUSIONS	39
REFERENCES	39

ILLUSTRATIONS

Figure		
1.	Polarization Direction Diagram	8
2.	Vacuum Chamber Schematic	12
3.	Optical and Electronic Arrangement for Electron Beam Measurements	12
4.	Schematic of Electron Gun Power Supply	13
5.	Signal-to-Noise Ratio versus Discriminator Voltage for EMI 6256 Photomultiplier Tube	15
6.	Signal-to-Noise Ratio versus Discriminator Voltage for ITT FW-130 Photomultiplier Tube	15
7.	Optical and Electronic Arrangement for Rayleigh Scattering Measurements	18
8.	Filter Transmission Curve	19
9.	Axial Profile of T_R/T_o - Low P_oD	23

Figure		Page
10.	Axial Profile of T_R/T_o - High P_oD	23
11.	Radial Variation of N_2 Rotational Temperature	24
12.	Isometric Profile of T_R/T_o of N_2	24
13.	Variation of T_R/T_o with Reservoir Pressure	26
14.	Low T_o Axial Profiles of T_R/T_o	26
15.	Radial Variation of N_2 Rotational Temperature, P_o = 100 Torr	27
16.	Radial Variation of N_2 Rotational Temperature, P_o = 500 Torr	27
17.	Rayleigh Scattering for P_o = 500 Torr	28
18.	Rayleigh Scattering for P_o = 1000 Torr	29
19.	Rayleigh Scattering for P_o = 1500 Torr	29
20.	Rayleigh Scattering for P_o = 2000 Torr	30
21.	Rayleigh Scattering for P_o = 3000 Torr	30
22.	Rayleigh Scattering for P_o = 4000 Torr	31
23.	Axial Variation of N_2 Rayleigh Scattering Measurements	31
24.	N_2 P-T Diagram	33
25.	Variation of Onset Location versus Reservoir Pressure	33
26.	Variation of Supersaturation Ratios with Reservoir Pressure	34
27.	Axial Extrapolation of T_R/T_o for Diabatic Flow Analysis	38

NOMENCLATURE 41

1.0 INTRODUCTION AND THEORY

1.1 BACKGROUND AND PREVIOUS MEASUREMENTS

The production of condensed, or two-phase, flow by means of a supersaturated, supersonic, or hypersonic expansion has been observed by many investigators. Because of an obvious desire to predict the onset of condensation in aerodynamic simulation facilities, Daum and Gyarmathy (Ref. 1) have attempted to correlate (with the nozzle source reservoir parameters) the observed pressure and temperature of both nitrogen and air at which onset occurs. Of a more fundamental nature, Wegener (Ref. 2) has studied homogeneous condensation processes in expansion flows with the goal of obtaining an understanding of the relationship between onset and subsequent condensate growth and molecular parameters. The approaches taken by the authors of both Refs. 1 and 2 are classical in the sense of using concepts of critical radii to describe the onset and growth processes, and both references contain excellent bibliographies of previous work using this approach. There has been a relatively recent revival of interest in this particular problem for a variety of reasons, including the possibility of the use of massive clusters or polymer beams for fusion applications, as well as interest in the possible enhancement of scattered intensity of radiation either incident upon, or emitted by, a plume containing clustered molecules. As a result of this interest, numerous studies of clustered or condensed molecular beams have resulted using either mass spectrometric (Refs. 3 and 4) detection of polymers in the free-molecular, far-field region of the plume or electromagnetic filters sensitive to the charge-normalized number of molecules per cluster (Ref. 5). Additionally, application has been made of both the electron beam fluorescence method (Refs. 6 and 7) and laser Rayleigh scattering method (Refs. 7 and 8) for diagnostics of two-phase flow fields, thereby obtaining even more detailed information concerning the spatial location of the onset of condensation. Finally, Raman scattering (Ref. 9) has been applied to the problem for the measurement of monomer gas density throughout the flow field, including the region of the onset of condensation. In view of the added measurement capabilities available, it is felt that the additional experimental parameters to be obtained by their use will provide more stringent tests of proposed theories of homogeneous condensation. Moreover, more detailed and extensive measurements of the condensation process are required for expansion flows in general and sonic orifice flows in particular to provide information concerning the scaling laws of the phenomenon with respect to orifice diameter, D; reservoir pressure, P_o; temperature, T_o; and gaseous specie. It should be noted that previous

results of mass spectrometric sampling have been used to provide scaling laws of sonic orifice flows with respect to D, P_o, and T_o. However, the very definition of the occurrence of condensation is not clearly delineated; e.g., Daum and Gyarmathy used the Wilson point criterion, while Golomb, et al. (Ref. 3) defined the onset of condensation, as observed in the farfield of the plume, by two criteria: (1) the occurrence of mass spectra peaks of dimers (which essentially coincides with the n-mer peak) and (2) a break in the flow speed curve when observed as a function of reservoir pressure. Wegener (Ref. 2) generally has employed the departure of the static pressure from the isentropic prediction, and Hagena and Obert (Ref. 5) prefer to scale according to constant values of (N/Z). Obviously, the definition of onset requires some care and must be chosen to reflect the ultimate application of the results, because all expansion flow fields which possess finite supersaturation will exhibit some degree of condensation, even if only in the form of dimer molecules.

It is the purpose of this work to provide new information concerning nitrogen (N_2) condensation in a sonic orifice expansion flow. Specifically, it is desired to obtain information concerning the spatial location of onset of condensation, estimates of the mass fraction of condensate, and information concerning both the spatial variation of the condensate growth and the dependence of these preceding items on reservoir pressure. Finally, with such information it is desired to compare these results with the far-field sampling techniques discussed in Refs. 3 and 4. For this comparison, it is of special interest to obtain information concerning the size range and number density of N_2 clusters and to attempt to correlate previous mass spectrometric observations with actual changes in the flow-field properties such as gas temperature. To accomplish this goal, it was decided to employ both the electron beam fluorescence technique for far-field, low-density gas temperature diagnostics and laser Rayleigh scattering for observation of the condensate growth. These flow diagnostic techniques will be briefly discussed in the two following sections.

1.2 ELECTRON BEAM FLUORESCENCE TECHNIQUE

The use of the fluorescence radiation resulting from inelastic electron-molecule collisions for the measurement of gas density and temperature in a hypersonic flow field has been demonstrated by many investigators (Refs. 10 through 12). Briefly, a high energy beam of electrons (with energy in the range of 10 to 50 kev) produces upon impact

with either atomic or molecular species excited electronic states. By radiative decay, these states produce a fluorescence, the intensity of which is directly proportional to gas density, assuming no collisional quenching effects. Furthermore, in the event of electron-molecule collisions, the molecular radiation consists of vibrational-rotational band structure within the electronic transition system, which, upon spectral separation, yields information concerning the temperatures of the internal energy modes or the energy distribution function. As described in Ref. 11, in the case of N_2 the electronic system used for such temperature measurements is the N_2^+ First Negative, N_2^+ (1-), and the (0, 0) vibrational band is spectrally resolved for determination of the rotational temperature, T_R, of the ground-state N_2 molecule. Clearly, observation of rotational temperatures in excess of those to be expected for the uncondensed, but rotationally relaxing, N_2 flow will be a manifestation of the heat release attributable to the recombination process of condensation and, thereby, a direct diagnostic for the onset of condensation. It should be noted that the electron beam-induced fluorescence spectra of the (0, 0) band of the N_2^+ (1-) system are interpreted using dipole selection rules for the electron-molecule ionization-excitation process.

1.3 RAYLEIGH SCATTERING

It is well known that the photon-molecule interaction can result in a scattering event for which the internal energy state of the molecule remains unchanged. The scattered photon is said to have experienced Rayleigh scattering, and the scattered photon energy is essentially the same as that of the incident photon. Assuming a laser source of intensity, I_o, and wavelength, λ, Fig. 1 shows the scattering configuration used in this study. It is to be noted that the incident beam is linearly polarized, and the polarization direction of the detector is aligned parallel to that of the incident beam. It is easily shown (Ref. 13) that the scattered intensity, I_s, from a collection of N molecules, each of polarizability α, is given by

$$I_s/I_o = K_\alpha \cdot N \cdot \alpha^2/\lambda^4 \tag{1}$$

where the constant factor K_α includes all optical transmission and sensitivity factors. As is known, the polarizability α for a spinless diatomic molecule is given by the trace of the polarizability tensor $\bar{\alpha}$

$$\mathrm{Tr}2 = \alpha = (1/3)(\alpha_1 + 2\alpha_2) \tag{2}$$

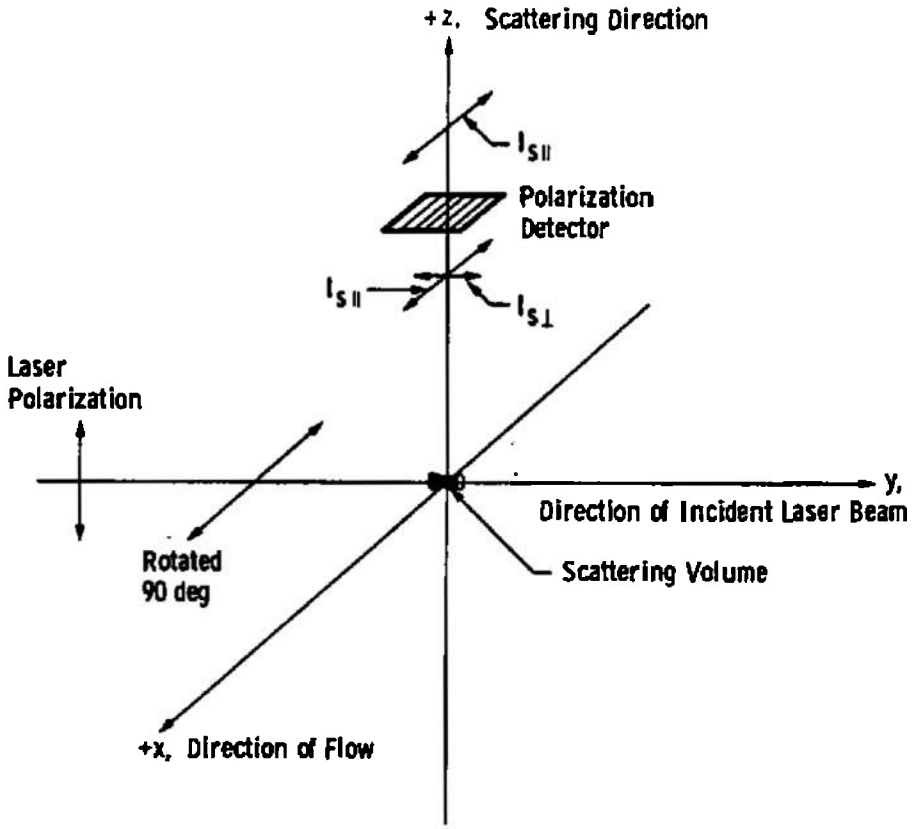

Figure 1. Polarization direction diagram.

where α_1, α_2, and α_3 represent the components of polarizability along the body axes of the molecule. To appreciate the value of Rayleigh scattering as a diagnostic for the onset and growth of condensation, one can simplistically imagine the scattering molecule to be a dielectric sphere of radius, a, and index of refraction, m. The polarizability α can be replaced by the expression (Ref. 13)

$$\alpha = (m^2 - 1)a^3/(m^2 + 2)$$

and Eq. (1) becomes

$$I_s/I_o = K_a \times N \times a^6/\lambda^4 \tag{3}$$

where

$$K_a = [(m^2 - 1)/(m^2 + 2)]^2 \times K_\alpha$$

If the scattering medium is characterized by a polydisperse size distribution, Eq. (3) becomes

$$I_s/I_o = (K_a/\lambda^4) < Na^6 > \tag{4}$$

where $<Na^6>$ is the expectation value of the product. One notes from Eq. (4) that upon onset of condensation the scatterer grows in size as clustering proceeds, and the scattering signal varies with the sixth power of the radius of the polymer. Therefore, using the simplistic view that a dimer is twice as large as a monomer, only 1.5 percent dimers in the flow will essentially double the scattering signal. Therefore, Rayleigh scattering is a very sensitive measurement for the existence of clusters in a condensing flow field. It should be noted that if the cluster size is such that $a/\lambda \lesssim 0.05$, the above description is adequate and the more complicated Mie scattering theory is not required (Ref. 14). Previous studies of condensation processes in an expansion flow indicate scatterer sizes on the order of 100 Å or less, and for visible laser wavelengths the Rayleigh equations are adequate.

Returning to the polarizability description of the scattering process, for a collection of polymers, the largest of which is designated as the j-mer, the scattered intensity Eq. (1) can be written as

$$I_s/I_o = (K_\alpha/\lambda^4) \times N_1\alpha_1^2 \left[1 + \sum_{i=2}^{j} (N_i/N_1)(\alpha_i/\alpha_1)^2\right] \tag{5}$$

For an expansion flow field it is desirable to nondimensionalize N_1 by use of the reservoir density, N_o, and Eq. (5) becomes

$$I_s/I_o = (K_\alpha \times N_o \times \alpha_1^2/\lambda^4)(N_1/N_o) \left[1 + \sum_{i=2}^{j} (N_i/N_1)(\alpha_i/\alpha_1)^2\right] \tag{6}$$

For small values of the mole fraction of condensate

$$N_1 \cong N_T = \sum_{i=1}^{j} N_i$$

and

$$N_i/N_1 \cong X_i = N_i/N_T$$

where X_i is the mole fraction of the i-mer.

Now

$$I_s/I_o = (K_\alpha \times N_o \times \alpha_1^2/\lambda^4)(N_1/N_o)\left[1 + \sum_{i=2}^{j} X_i(\alpha_i/\alpha_1)^2\right] \tag{7}$$

For a sonic expansion, the ratio N_1/N_o is given by the Sherman-Ashkenas equations (Ref. 15) if the expansion is isentropic. Assuming $\Delta S = 0$, N_1/N_o is a function only of the axial distance x/D and the specific heat ratio, γ. Therefore, for no condensation and relaxation, the axial variation of I_s/I_o is calculable, and any deviation from the predicted variation can be attributed to a nonisentropic rate process, the type of which is indicated by the variation of the deviation with P_o. Assuming the deviation from the (change in entropy) $\Delta S = 0$ prediction to be due to onset of nonequilibrium condensation, it is seen that the difference between the measured and predicted values yields an experimental measurement of

$$\sum_{i=2}^{j} X_i(\alpha_i/\alpha_1)^2$$

If one considers flow fields for which only dimers and monomers exist and assumes N_1 approximately equals the total number density, the equation for I_s/I_o becomes

$$I_s/I_o = (K_\alpha \times N_o \times \alpha_1^2/\lambda^4)(N_1/N_o)[1 + X_2 \times (\alpha_2/\alpha_1)^2] \tag{8}$$

so that values of X_2 can be obtained from measured values of I_s/I_o only if an estimate of α_2/α_1 can be found. Assuming additivity of bond polarizabilities and recognizing the weakness of the van der Waals binding of nitrogen dimers (Ref. 13), it seems reasonable to assume that α_2 is approximately equal to twice α_1. Thus, Eq. (8) becomes

$$I_s/I_o = (K_\alpha \times N_o \times \alpha_1^2/\lambda^4)(N_1/N_o)[1 + 4X_2] \tag{9}$$

Consequently, for low values of condensate mass fraction, for which N_1/N_o is approximately equal to its $\Delta S = 0$ value, the scattering signal excess to the isentropic prediction is an approximate measure of the dimer mole fraction, X_2.

2.0 EXPERIMENTAL APPARATUS AND METHOD

2.1 GAS SOURCE AND VACUUM CHAMBER

The flow field was produced by a tubular sonic orifice source of 3-mm orifice diameter and 0.013-cm thickness, a diameter-to-thickness ratio of approximately 24. The source was constructed of stainless steel tubing of approximately 1-cm inside diameter and 10-cm length. Copper cooling coils were wound around the source to provide temperature variation, by means of flowing either liquid or gaseous N_2 through the coils, and several strips of Nichrome® were wound atop the cooling coils to aid thermal control. The source was designed so that the ratio of the residence time within the source and the rotational relaxation time was several orders of magnitude greater than unity to ensure thermal equilibration. The source was provided with copper-constantan thermocouples and a calibrated pressure gage for T_o and P_o measurements, respectively. All data were obtained using prepurified N_2 with a stated purity of 99.998 percent, and particulate filtering was accomplished using two Millipore® 0.025-μm filters arranged in parallel.

The gas source was mounted on a three-dimensional traversing mechanism, the description of which is given in Ref. 8, as is the description of the vacuum chamber itself. The traversing mechanism has an accuracy and reproducibility of 0.013 cm in the axial direction. The vacuum chamber, which enclosed the motor-driven traversing mechanism, was maintained at background pressures of 10^{-6} torr or less with no gas flow and 10^{-5} to 10^{-4} torr with maximum gas flow, and Fig. 2 shows a section view of the chamber. The low background pressure, P_B, with mass flow rates exceeding 1 gm/sec was maintained by liquid N_2 and gaseous helium (He) cryopumping liners. Background pressures were measured using calibrated ionization gages, and the ratio P_o/P_B was 10^5 or greater for all cases. Fluctuations in P_o and T_o during the course of data acquisition were each on the order of one percent or less.

2.2 ELECTRON BEAM APPARATUS

Optical and electronic components used in the electron beam measurements are shown in Fig. 3. The electron source was Radio Corporation of America (RCA) model VC2126 V4 electron gun mounted

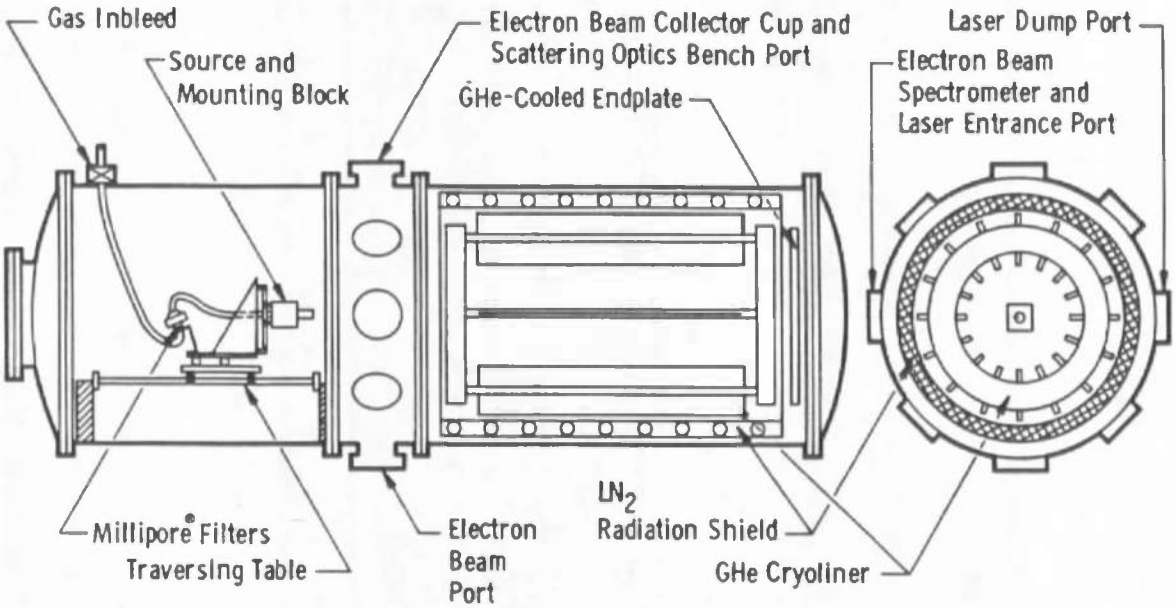

Figure 2. Vacuum chamber schematic.

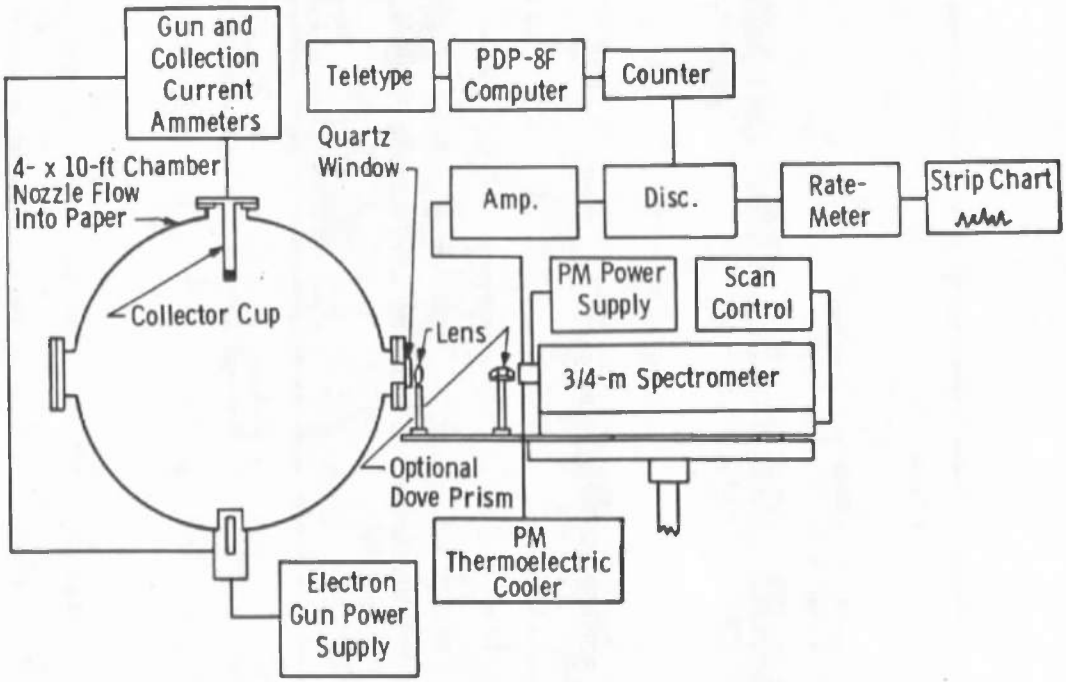

Figure 3. Optical and electronic arrangement for electron beam measurements.

in a stainless steel housing at the bottom of the chamber, and the beam was directed vertically upwards. The beam was injected into the chamber and flow field through a 1.0-mm-diam orifice and was magnetically focused to provide a sufficiently small diameter beam source at the centerline of the cell and flow field. The chamber centerline was located approximately 50 cm from the injection orifice. A 15-cm diffusion pump with a liquid-N_2-cooled baffle maintained the electron gun pressure at less than 2×10^{-5} torr. The electron gun power supplies and voltage dividing network are shown in Fig. 4. All measurements used a potential of 40 kv. The beam collector cup was similar to that described and shown in Ref. 16, except that its length was 34 cm. The distance from the plume axial centerline to the first grid of the collector cup was 30 cm. Vertical alignment of the gun exit orifice, collector cup, and pitot probe, which served as a plume centerline reference point, was performed with a plumb bob.

The beam fluorescence was focused onto the 20-μm-wide entrance slit of a 0.75-m Spex scanning spectrometer with a 1200-groove/mm, 3000-Å blaze grating and operated with equal entrance and exit slit widths. The 25.4-cm focal length lens was apertured to a diameter of 4.5 cm to match the spectrometer f-number. Scan rates were varied from 1 to 3 Å/min. The slower rates were required for adequate line peak duration times in low-density flow regions.

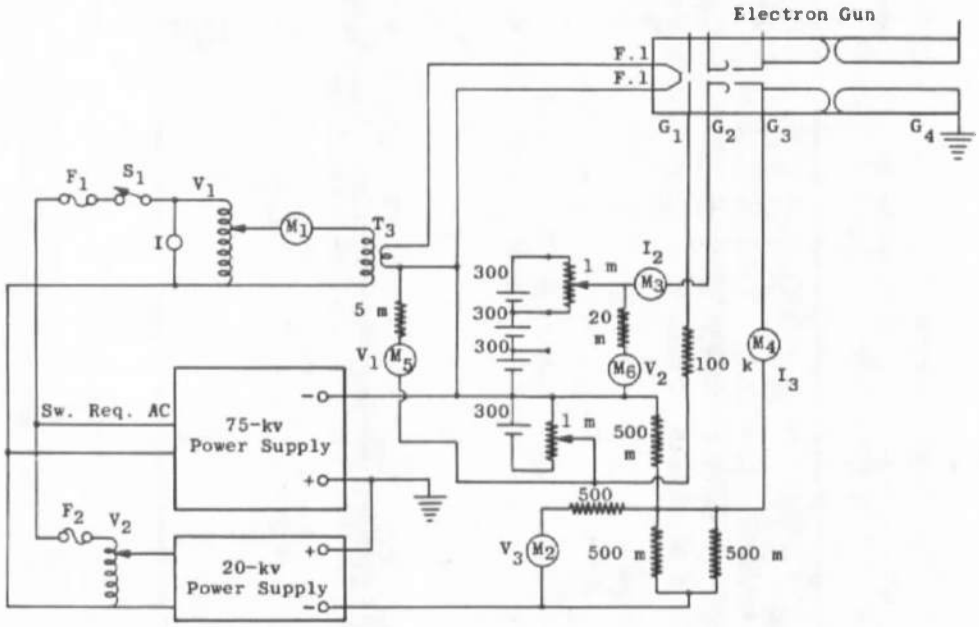

Figure 4. Schematic of electron gun power supply.

During the course of the measurements, T_R data were acquired with both the spectrometer slit parallel to the electron beam and, by use of a Dove prism, perpendicular to the beam. The slit heights were 1 to 3 mm and 6 mm, respectively, and the respective magnification factors were 1.6 and 1.8. To the accuracy of the measurement, no systematic differences in the results for T_R were noted with the two configurations, and it must be concluded that no systematic effects of flow-field gradients are present in these results.

A Calibration Standards Corporation power supply provided 1500 v to the EMI 6256S photomultiplier tube and 1800 v to the International Telephone and Telegraph (ITT) FW130 photomultiplier tube. The 6256S tube has an "S"(Q) spectral response and is designed for very low light levels in the near ultraviolet. The FW130 has an S-20 spectral response and is also particularly suited for photon counting applications. Figures 5 and 6 show signal-to-noise ratios as a function of discriminator voltage for a 6256B tube at its operating temperature of -20°C and for the FW130 tube at -30°C. The behavior of the 6256S is close to that of the 6256B. Discriminator voltages of 0.6 v for the 6256S and 0.5 v for the FW130 were selected for an optimum balance between count rates and sufficiently high signal-to-noise ratios. The signal-to-noise ratios are greatly improved at cold temperatures.

In obtaining a temperature from a scan, no spectral sensitivity corrections were necessary since only relative peak heights are required in a narrow wavelength interval.

The photon counting system consisted of the following Ortec instruments: Model 454 timing filter amplifier, Model 436 100-MHz discriminator, Model 441 ratemeter, and Model 715 dual counter/timer. A 50-ohm photomultiplier output load resistor and maximum amplification of the electronic processing system were used. Two methods of data recording were employed. For the first method a Digital Equipment Corporation PDP®-8F computer was used to acquire the output data from the counter/timer. The second method consisted of a Honeywell Electronik 19 strip-chart recorder registration of the analog output of the ratemeter.

The PDP data acquisition program employed included provisions for spectral background measurements, measurement of R-branch peak amplitudes and wavelengths, real-time calculations of rotational temperatures, and normalization of the data for variation of the electron beam current.

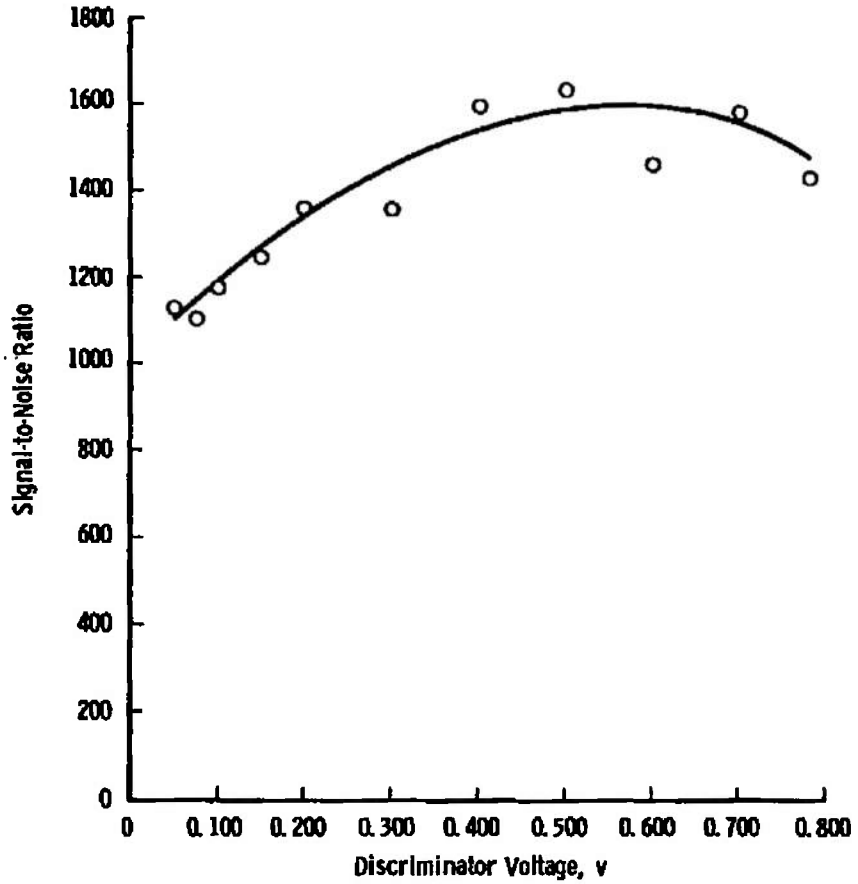

Figure 5. Signal-to-noise ratio versus discriminator voltage for EMI 6256 photomultiplier tube.

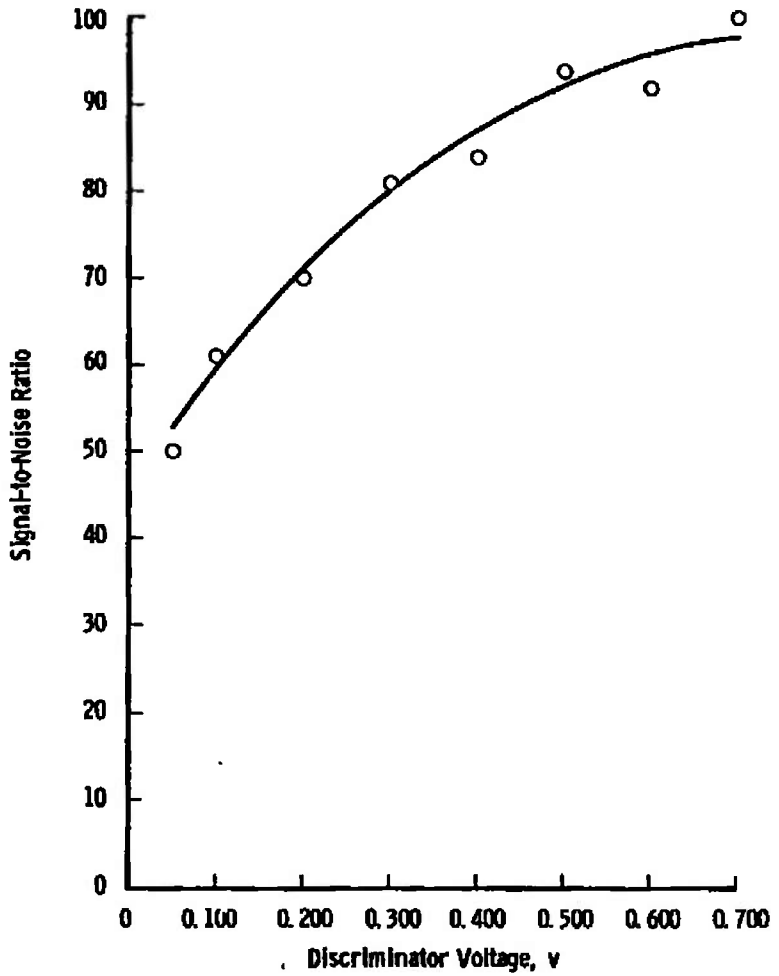

Figure 6. Signal-to-noise ratio versus discriminator voltage for ITT FW-130 photomultiplier tube.

The spectrometer data were acquired through the digital input buffer from the Ortec photon counting equipment. A variable sampling interval was available and chosen for compatibility with the spectrometer scanning speed and signal intensity. The line wavelength was determined from the time measurement which was read into the computer along with the spectrometer data. The Ortec B counter was used in the 0.1-sec clock mode. The spectrometer starting wavelength and scan speed were manual inputs via the keyboard such that the wavelength of the individual lines could be identified.

An average background count was determined by count accumulation for several sampling intervals and simply dividing by the number of samples taken. A background wavelength interval was specified via the keyboard. Similarly, the wavelength interval for a temperature measurement was input to the computer.

The line amplitudes were determined by selecting the maximum value that existed between a specified number of monotonically increasing samples and a similar number of monotonically decreasing samples. The number of samples to identify a positive and negative slope was variable and generally chosen as three. This approach was taken to isolate false peaks attributable to noise. Although three samples for a slope identifier occasionally gave false peaks, this number of samples was chosen for sensitivity purposes. Real and false lines were identifiable by inspection of the associated wavelengths.

For the purpose of obtaining real-time temperature results from the spectral data ratios of individual R-branch rotational line intensities of the $N_2^+(1-)(0,0)$ band were used. Theoretical calculations of the electron beam-induced fluorescence of the $N_2^+(1-)(0,0)$ band were performed using the spectrometer dispersion, entrance and exit slit width values. Ratios of the rotational line intensities of the K = 1 and 3 levels and 3 and 7 levels were expressed as a function of T_R over the T_R ranges of 10 to 70°K and 50 to 150°K, respectively. The rotational temperature was calculated on-line by the computer using the equations

$$T_R = \frac{18.7}{0.985 + \ln \frac{R(1)}{R(3)}} \qquad 10 \text{ to } 70°K$$

$$T_R = \frac{107}{0.753 + \ln \frac{R(3)}{R(7)}} \qquad 50 \text{ to } 150°K$$

where R(1), R(3), and R(7) are the rotational line intensities of the transitions from the K = 1, 3, and 7 rotational levels, respectively. Sufficient computer storage was not available to use multiple line least squares curve fits for temperature determination. However, the above curves were adequate to the extent that temperature errors less than 2°K were obtained when compared to least squares calculations.

Background corrected peak heights of the emission lines were used in computer program TROT (Ref. 16) to calculate the rotational temperature from the Boltzmann plot as described in the previous reference to the experimental data.

Using analog recording at each position in the flow for which data were acquired, background deflections for each scale position of the ratemeter were recorded at 3918 Å. This wavelength location was devoid of any impurity radiation and yet only 4 Å from the 3914 Å (0, 0) bandhead, thereby precluding any wavelength dependent effects on the background measurement. The spectral scan was begun at approximately the band origin at 3910 Å, and scanning was concluded at approximately 3900 Å.

The ratemeter scale factors were selected to obtain maximum chart deflections for each line, and the ratemeter was linear over the ranges selected. The time constant associated with the standard deviation selector of the ratemeter was kept equal to or less than 0.5 sec. Because the time constant is a function of the scale factor, the two switches were changed together. As in the PDP-8 analysis, program TROT was used to obtain the temperature from the resultant line peak heights. A computer program that weighted each line according to its intensity and calculated a rotational temperature was developed for this latter part of the measurements. Since stronger lines had larger signal-to-noise ratios, more weight was given to them. The rotational temperature from a five-line weighted average was generally taken.

2.3 RAYLEIGH SCATTERING APPARATUS

The optical and electronic experimental arrangement for the Rayleigh scattering measurements is shown in Fig. 7. The laser source employed was a Coherent Radiation Model 52-B argon-ion laser operating at a wavelength of 4880 Å and a power of 0.5 w. A 1/2-wave plate was used to rotate the normal vertical polarization of the laser output to

horizontal polarization (the polarization vector is into the plane of Fig. 7). A quartz lens of 3.81-cm diameter and 1-m focal length focused the laser beam through a quartz chamber window and a series of three 0.48-cm-diam apertures to a point approximately on the chamber centerline. The final aperture was located 30.5 cm from the laser beam focal region. As the laser beam defocused, it entered a laser dump, the entrance of which was a black cardboard tube which extended into the chamber to within 22.5 cm of the chamber centerline. The latter stage of the dump was a black anodized aluminum tube capped with a black anodized conical section.

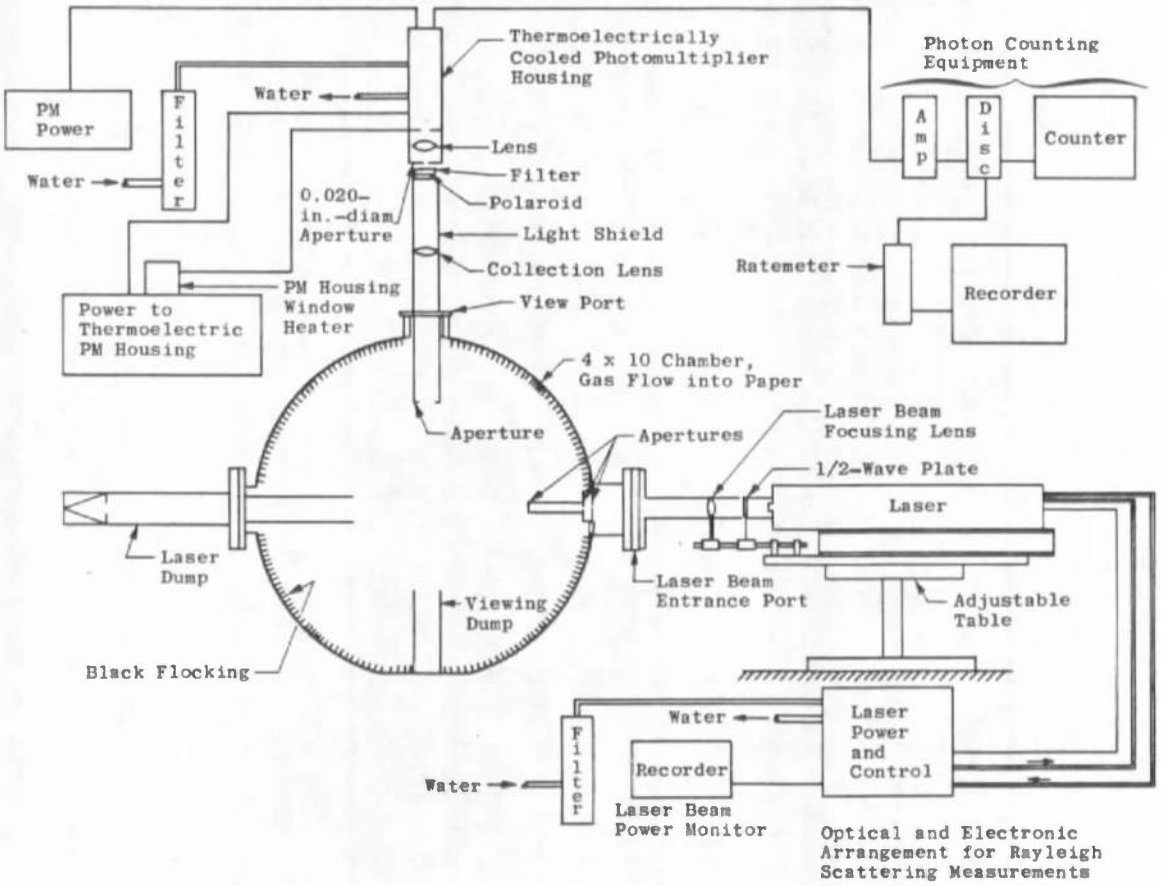

Figure 7. Optical and electronic arrangement for Rayleigh scattering measurements.

The focal region of the laser beam was located at the focal point of the collection optics system which was oriented at 90 deg with respect to the flow-field axis and laser beam. The scattering volume was viewed through a glass port by a glass lens of 12.7-cm-diam and 24-cm focal length. The collected Rayleigh scattered radiation was transmitted through a small piece of HN-22 Polaroid® material

with the polarization transmission axis usually parallel to that of the laser beam and then through a 4880-Å pass interference filter of 10-Å half-width (see Fig. 8 for transmission curve). The radiation was focused onto a 0.0508-cm-diam aperture, and light passing through the aperture was focused by a small lens onto the photocathode of an ITT FW130 photomultiplier tube mounted in a thermoelectrically cooled housing and cooled to -26°C.

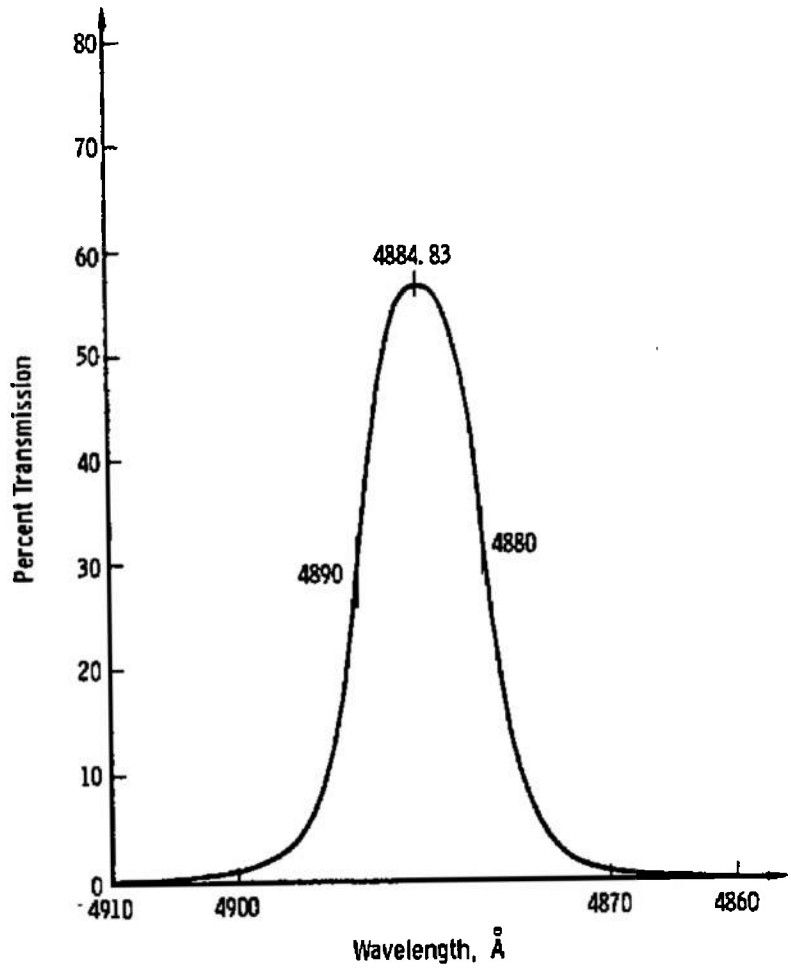

Figure 8. Filter transmission curve.

The collection optics system was shielded with black cardboard and shrouded with layers of green felt. For further reduction of stray light, a collection optics viewing dump, consisting of a piece of black cardboard tubing, was located at the bottom of the test chamber collinear with the scattering volume and the center of the collection lens. All optically accessible surfaces inside the test chamber,

including the sonic orifice source, were either painted with a flat black coating or covered with a black flocking material. An additional 25.4-cm length of black cardboard tubing was attached to the interior side of the collection optics viewport, and a 3.8-cm-diam aperture was mounted on the end of this tube to restrict the field of view of the collection optics.

The combination of input laser beam optics and collection optics provided a spatial resolution of approximately 1 mm^3.

Photon counting was used to process the photomultiplier tube output signal which was proportional to the scattered light intensity, I_s. The photomultiplier output was coupled through a 50-Ω load resistor to an Ortec photon counting system. Counting time intervals were preset for either 300, 100, or 10 sec.

The discriminator setting was such to maximize the signal-to-noise ratio, and the overall linearity of the system had been previously verified. The counting rates encountered during the investigation were sufficiently low relative to the 20-MHz capability of the system that no pulse pile-up effects existed. Finally, linearity of the signal with laser power had been verified, and the observed fluctuations in incident laser beam intensity were negligibly small.

Alignment of the laser beam focal volume with the focal point of the collection lens was necessary before actual scattering measurements began. Initially, the small diameter pitot probe was swung into a position that placed it on the centerline of the test chamber. A small incandescent light with frosted bulb was placed just below the tip of the pitot probe with the flat, top surface of the bulb just touching the underside of the probe tip, and the center of the circular bulb face was located 0.318 cm from the probe tip and collinear with the probe. Collection optics were adjusted in such a manner that the image of the lighted bulb was in focus and centered on the scattering volume defining aperture (an 0.0508-cm-diam pinhole). With the lightbulb removed, and the laser operated at low power, the laser beam focal volume was positioned 0.318 cm from the probe tip and on the axis of the pitot probe. With the laser operating at high power, and with cigarette smoke blown gently into the focal region, the laser beam focal volume was visually aligned with the scattering volume defining aperture by slight angular adjustment of the collection lens.

In order to relate the measured relative scattering intensity, (I_S/I_O), to values of $<N\alpha^2>$ and N, calibrations had to be performed. For each calibration, the test chamber was evacuated at room temperature. After the chamber pressure had decreased below 0.05 torr, the laser was operated at 0.5 w and the background (or zero pressure) relative intensity was observed.

After valving off the chamber vacuum pumps, nitrogen was slowly leaked into the chamber through the free-jet gas flow system. Rayleigh scattering intensity measurements were made at pressures of 200 and then 400 torr, as indicated by a calibrated Wallace and Tiernan gage. At the 200-torr point, the collection lens was adjusted slightly to maximize the collected radiation passing through the defining aperture. The calibration signal of the background adjusted Rayleigh scattering was linear with pressure at constant temperature.

Initially, calibrations were performed to determine the constant K_α in Eq. (5) using a gas sample for which N_1 was known and no clusters existed. Nitrogen at 280 K and 200 torr was used for the N_2 density reference point. However, it was found during the course of the measurements that the calibration factor determined thusly exhibited variations from day to day as a result of small disturbances to the optical train as well as variations of position during the evacuation and cooling of the vacuum chamber. Consequently, it was decided to use the flow field of the sonic orifice for calibration purposes. To do so requires that the axial position at which the calibration, or normalization, is performed be described by the Sherman-Ashkenas equation (Ref. 15) for N/N_o as a function of x/D, that the flow field not be saturated and that no rotational relaxation effects be present. The axial position used for calibration was chosen to satisfy these criteria, and the points so selected are denoted on the figures presenting these results as reference points.

Before actual flow-field measurements could begin, the location of the free-jet orifice relative to the observed scattering volume had to be accurately known. The axial location of the exit plane was readily determined by axially traversing the free jet in 0.01-in. (0.0254-cm) steps toward the laser beam path until the side of the free jet just touched the laser beam and prevented its passage across the test chamber. With the chamber at atmospheric pressure, the axial zero position was easily observed. The vertical and radial zero positions were measured by establishing a free-jet flow field, making vertical and radial intensity profile measurements and determining the zero positions from the flow-field symmetry.

The measurement procedure using the photon counting system was as follows:

1. The free-jet position was set and recorded,
2. With no gas flow and the chamber evacuated to 10^{-5} torr or less, a background relative intensity measurement was made, and
3. With the free-jet flow stabilized at the desired reservoir pressure and temperature, Step 2 was repeated, and the number of photon counts per second minus the background signal gave the Rayleigh scattered relative intensity in counts per second.

3.0 RESULTS AND DISCUSSION

3.1 ROTATIONAL TEMPERATURE RESULTS

Rotational temperature measurements were performed using the previously described electron beam fluorescence technique. The reservoir pressure was varied over the range of 100 to 1000 torr at 300 K reservoir temperature, and both axial and radial spatial surveys were performed. Figure 9 shows the axial variation of the 100 torr, or P_oD value of 300 torr-mm, results, and shown for comparison are the results of Marrone (Ref. 12) obtained for P_oD equal to 250 torr-mm. The isentropic curve from Ref. 15 is also shown, and the difference between the values of T_R/T_o and T/T_o has been shown conclusively by Marrone to be attributable to rotational relaxation effects. The 1500- and 3000-torr-mm axial variations are shown in Fig. 10, and Figs. 11 and 12 show the radial profiles of T_R/T_o for the 300-torr-mm condition. Figure 11 shows for comparison purposes for the x/D = 6 profile, data reported by Marrone for x/D = 6.3 and P_oD = 250 torr-mm. The agreement is good, although there is an increasing systematic difference in results as the radial distance increases. This difference is most likely real and is due to the different values of ratios of reservoir pressure, P_o, to background pressure, P_B, used in the two measurements. The data of Ref. 12 were acquired for the range $200 \lesssim P_o/P_B \lesssim 1500$, whereas the present data were acquired with $P_o/P_B \simeq 10^6$. Consequently, the present sonic orifice flow field most likely experienced greater expansion and, therefore, lower temperatures near the jet "boundary."

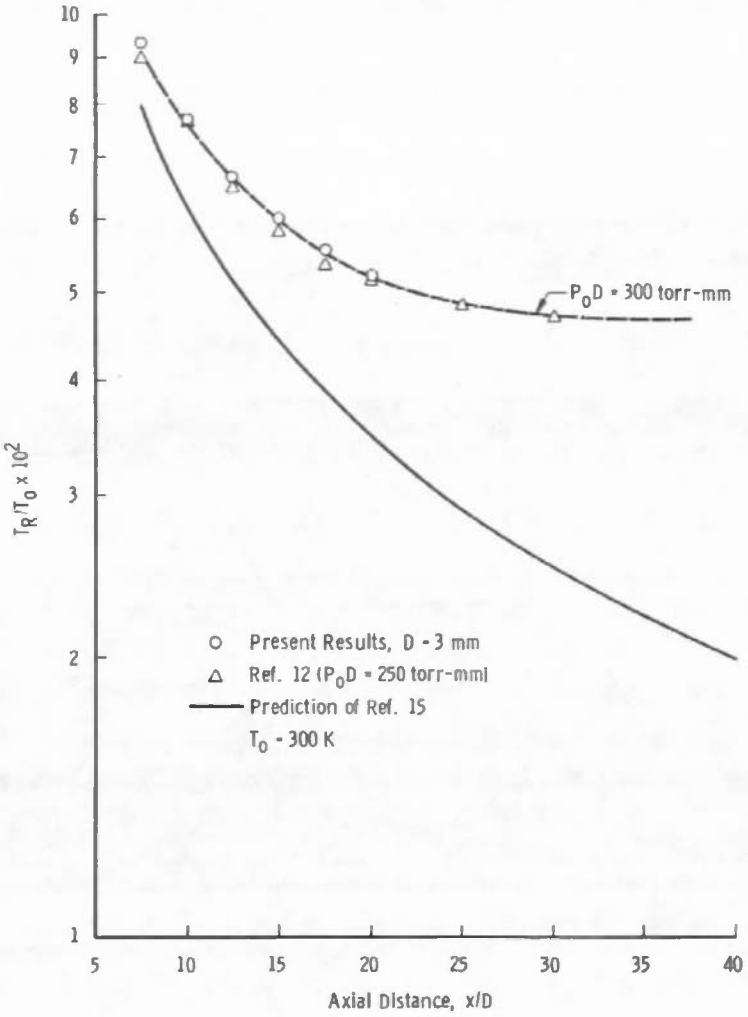

Figure 9. Axial profile of T_R/T_o - low P_oD.

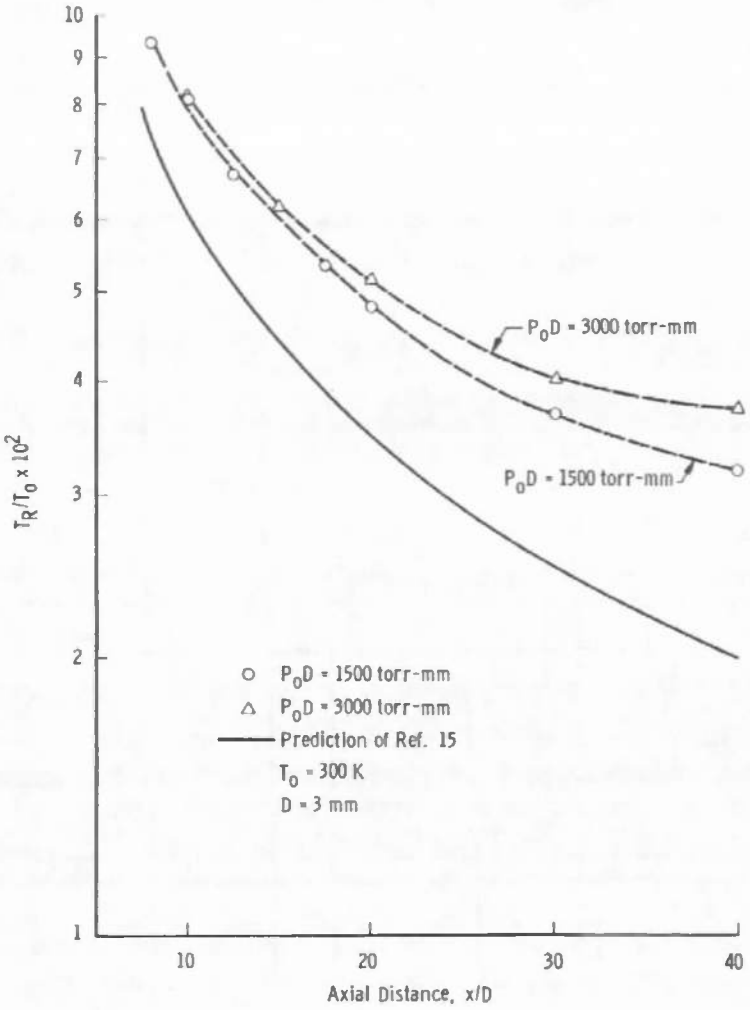

Figure 10. Axial profile of T_R/T_o - high P_oD.

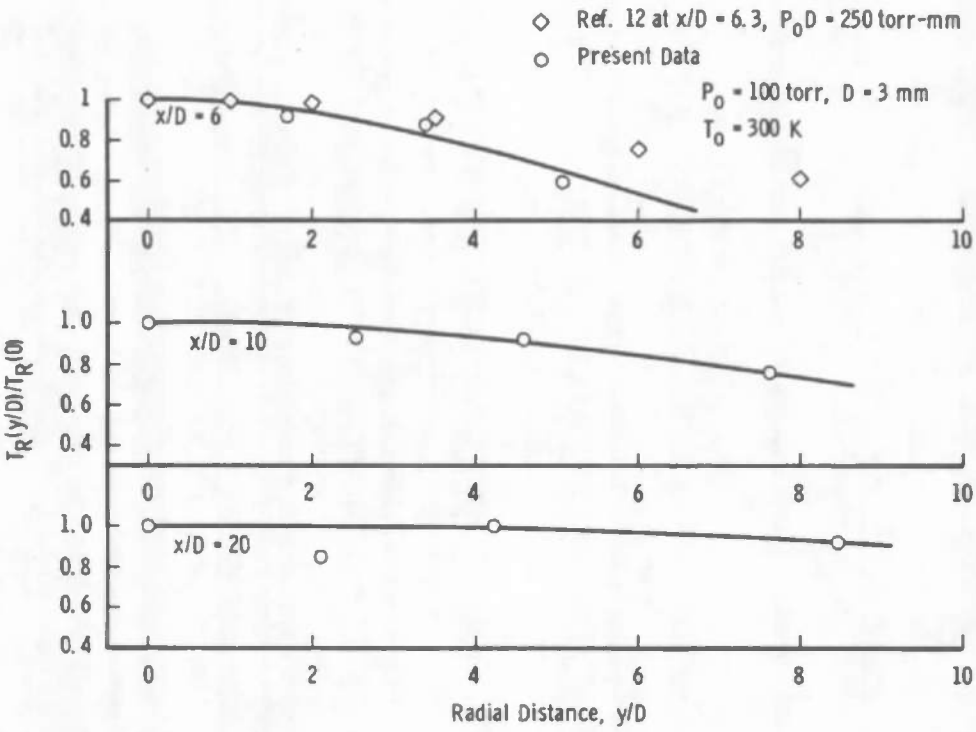

Figure 11. Radial variation of N_2 rotational temperature.

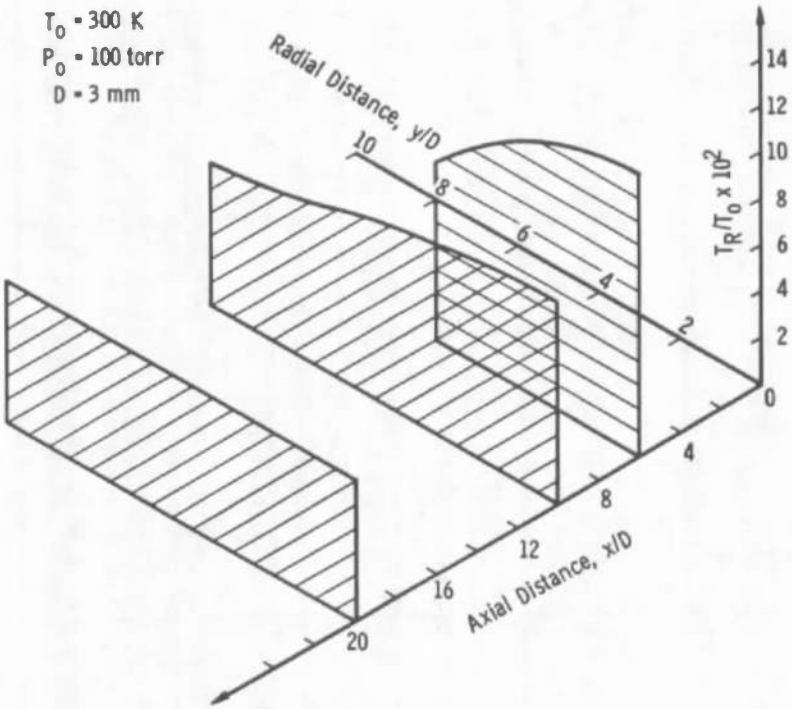

Figure 12. Isometric profile of T_R/T_o of N_2.

To determine the value of P_o at which condensation onset occurred within the flow, measurements of T_R were made at discrete axial positions over a wide range of P_o values. It was obvious that at low values of P_o rotational relaxation resulted in values of $T_R/T_o > T/T_o$, and as P_o increased the effect of binary collisional energy transfer decreased this difference in temperatures. In principle, neglecting all other effects,

$$\lim_{P_o \to \infty} (T_R/T_o) = T/T_o$$

However, at some value of P_o condensation onset occurs, and the heat of recombination increases the value of T_R/T_o once more. Therefore, one should observe a minimum in the value of T_R/T_o when observed as a function of P_o.

This series of measurements was performed at x/D = 15, 20, and 30. Figure 13 shows the results. The asymptotic limiting values of the T/T_o curve are shown at $P_oD = 10^4$ torr-mm. Using the values of T_R/T_o determined for the uncondensed, rotationally relaxing flow fields, a curve was extrapolated to the high pressure limit, which is the isentropic prediction of Ref. 15. Deviation of the measured value of T_R from this extrapolated curve is considered as a manifestation of the onset of condensation. For these three axial positions of x/D = 15, 20, and 30, the average onset pressure was found to be for the 3-mm-diam orifice

$$(P_o)_\theta = 290 \pm 50 \text{ torr}$$

Data were acquired for the axial variation of T_R/T_o at T_o = 116 K and P_o = 100 torr and T_o = 133 K and P_o = 500 torr. Figure 14 shows the result.* Additionally, radial variations at x/D = 6, 10, and 20 were obtained for both cases for the purpose of investigating any overall plume characteristic changes for flow fields which were obviously condensed. These results are shown in Figs. 15 and 16.

---

*The data of Fig. 14 have been corrected for rotational relaxation effects, as shown, assuming a temperature-independent rotational relaxation time and source Knudsen number scaling of the 300 K data of both Ref. 12 and the present work.

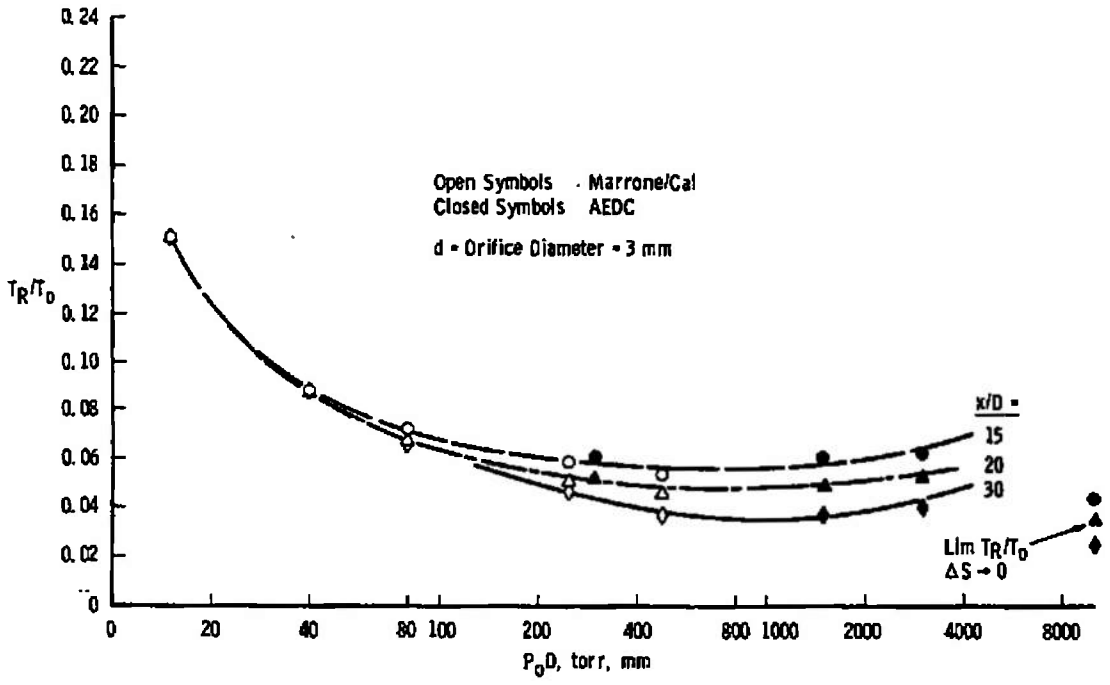

Figure 13. Variation of T_R/T_o with reservoir pressure.

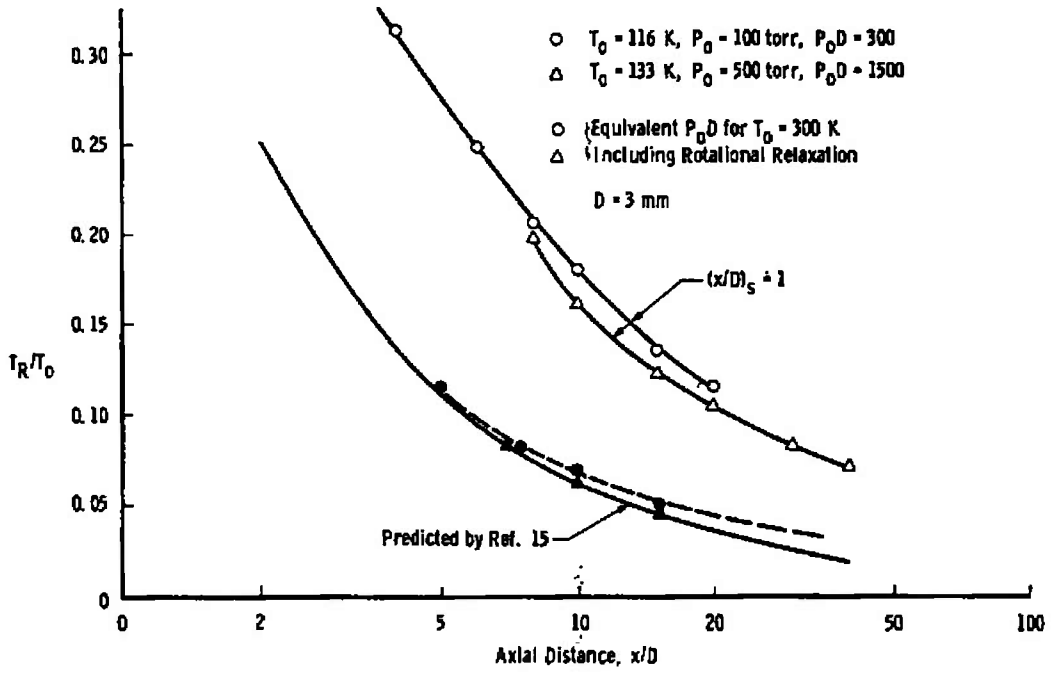

Figure 14. Low T_o axial profiles of T_R/T_o.

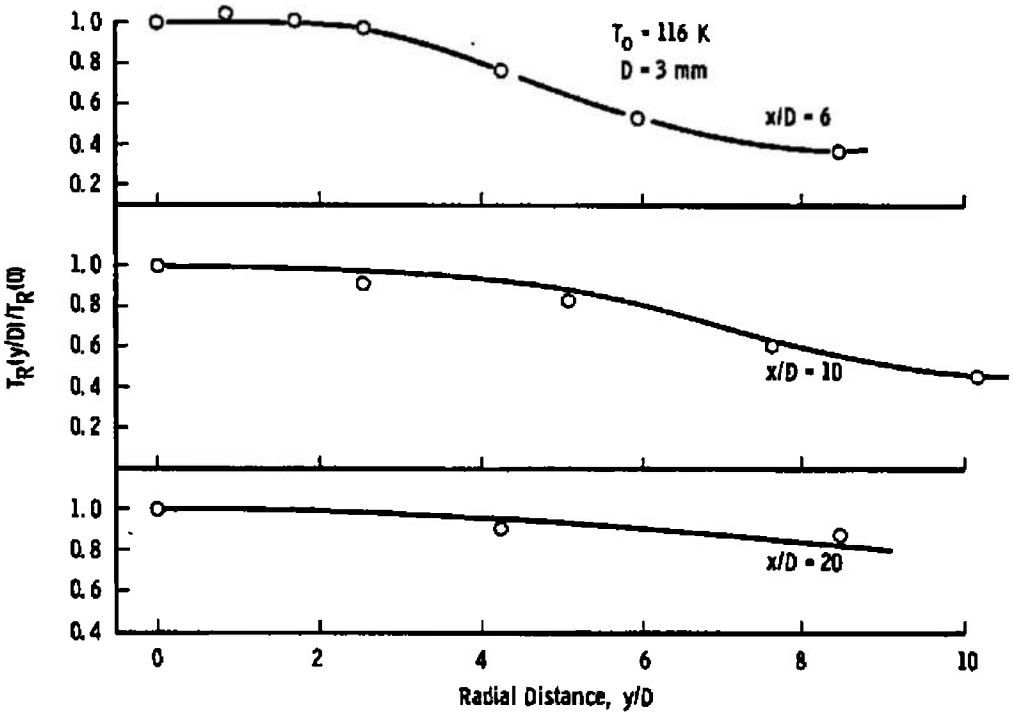

Figure 15. Radial variation of N_2 rotational temperature, P_o = 100 torr.

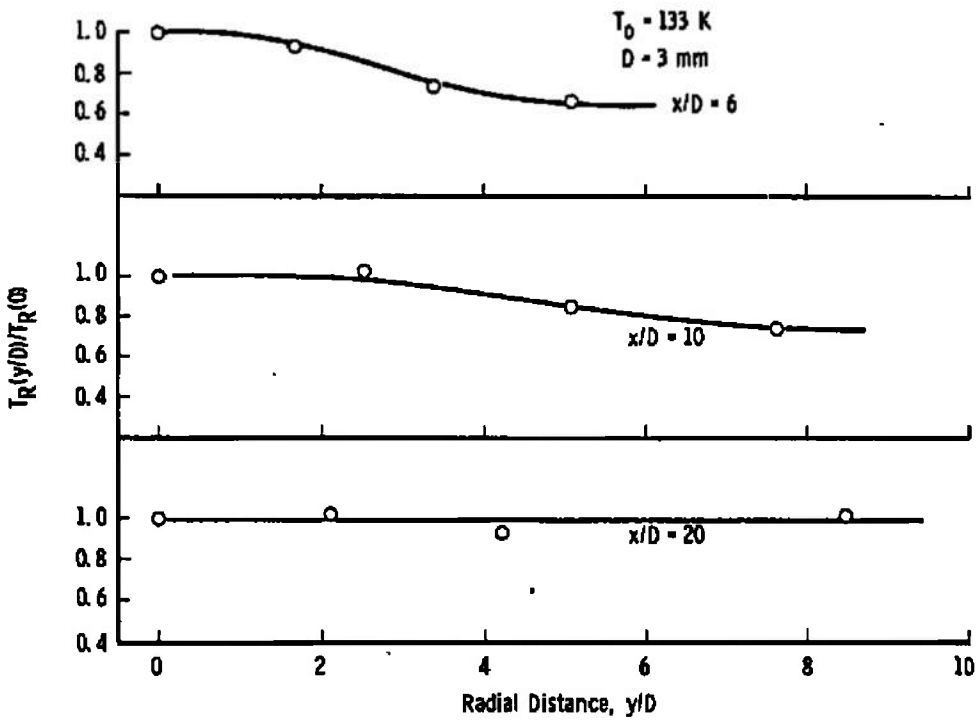

Figure 16. Radial variation of N_2 rotational temperature, P_o = 500 torr.

3.2 RAYLEIGH SCATTERING RESULTS

Axial variations of the scattering signal I_s/I_o were obtained for reservoir pressures 500, 1000, 1500, 2000, 3000, and 4000 torr. These results are shown in Figs. 17 through 22, and Fig. 23 shows all results on a single plot. The value of $(N_1/N_o)_{\Delta S=0}$ as predicted by the Sherman-Ashkenas equation (Ref. 15) is shown in each figure. The deviation of the data from this curve is evident for $P_o \geq 1000$ torr, and indicates the axial location of the onset of condensation, $(x/D)_\theta$. The agreement between the data and the predicted values for $1 \lesssim x/D < (x/D)_\theta$ as shown in Figs. 17 through 23 is to be noted.

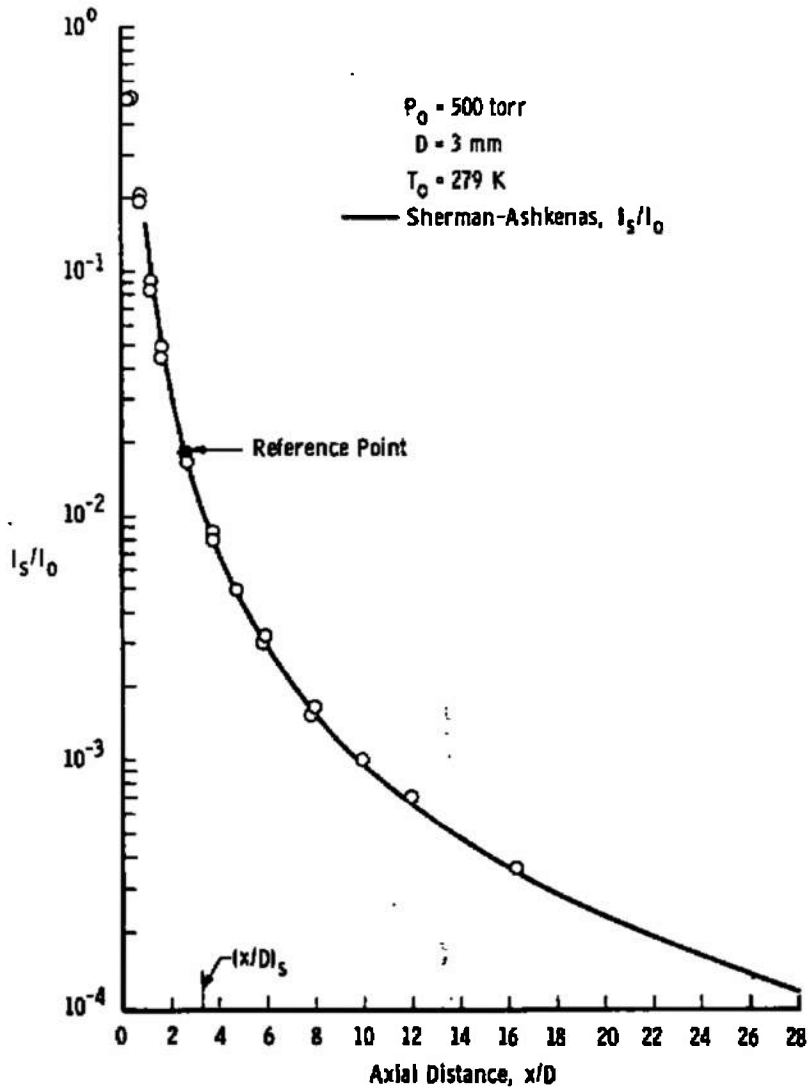

Figure 17. Rayleigh scattering for P_o = 500 torr.

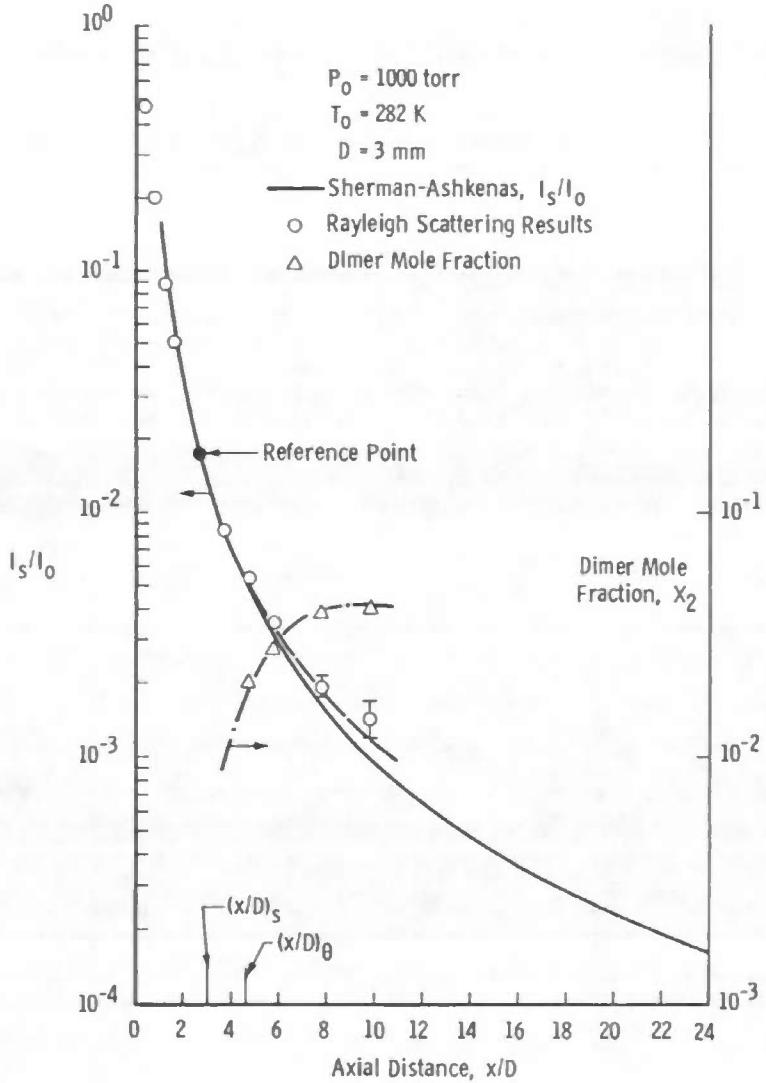

Figure 18. Rayleigh scattering for P_o = 1000 torr.

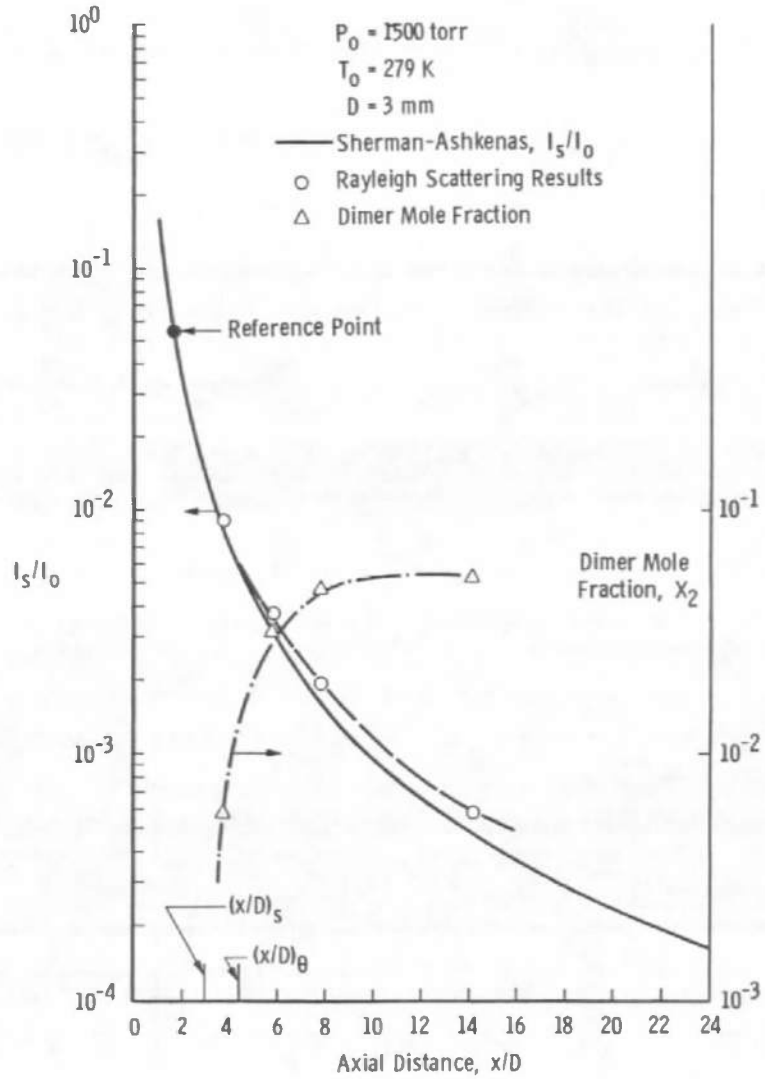

Figure 19. Rayleigh scattering for P_o = 1500 torr.

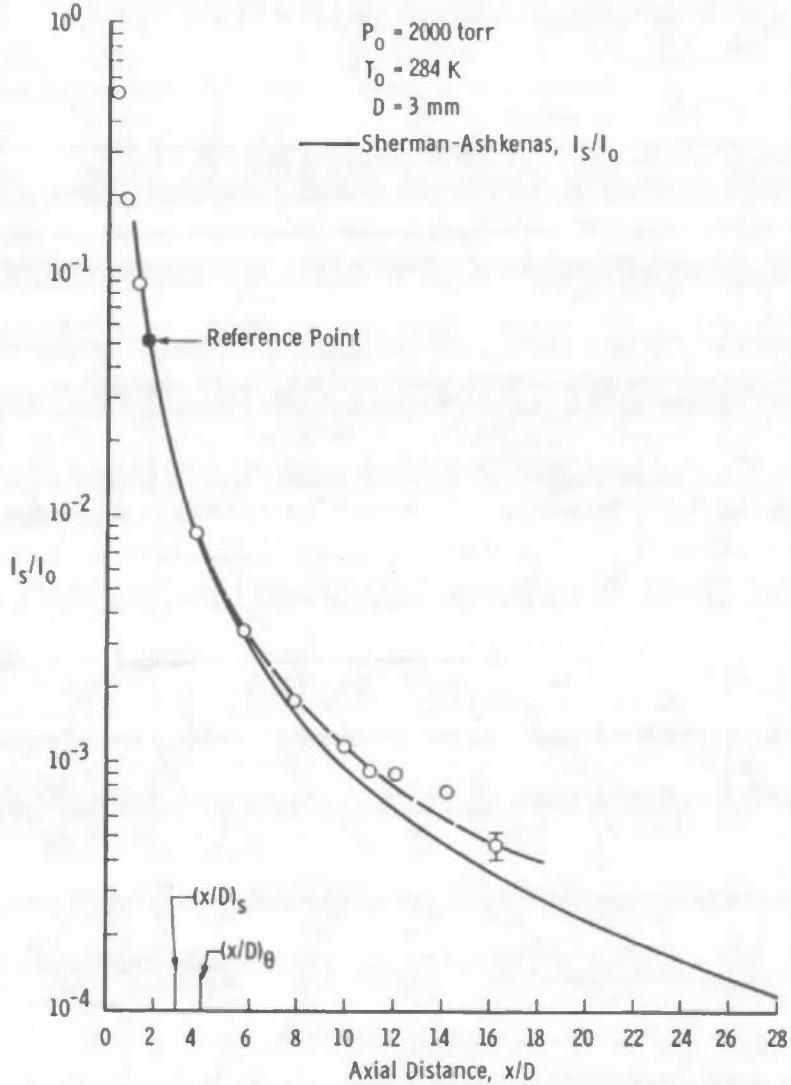

Figure 20. Rayleigh scattering for P_o = 2000 torr.

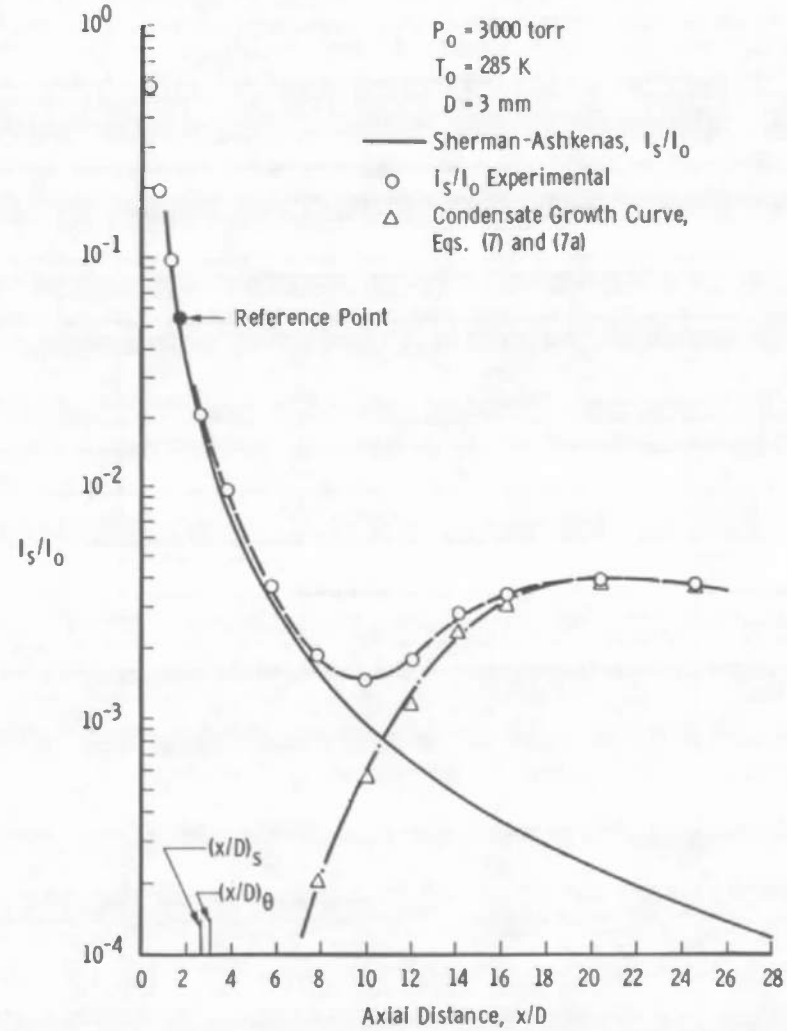

Figure 21. Rayleigh scattering for P_o = 3000 torr.

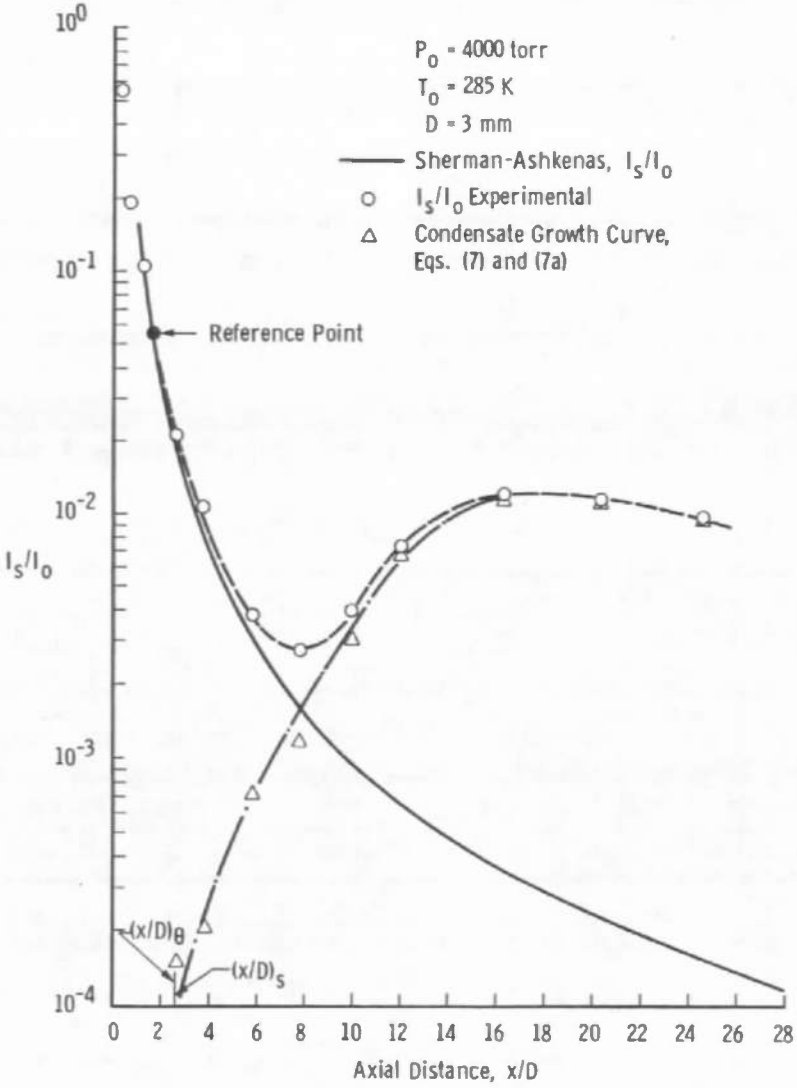

Figure 22. Rayleigh scattering for P_o = 4000 torr.

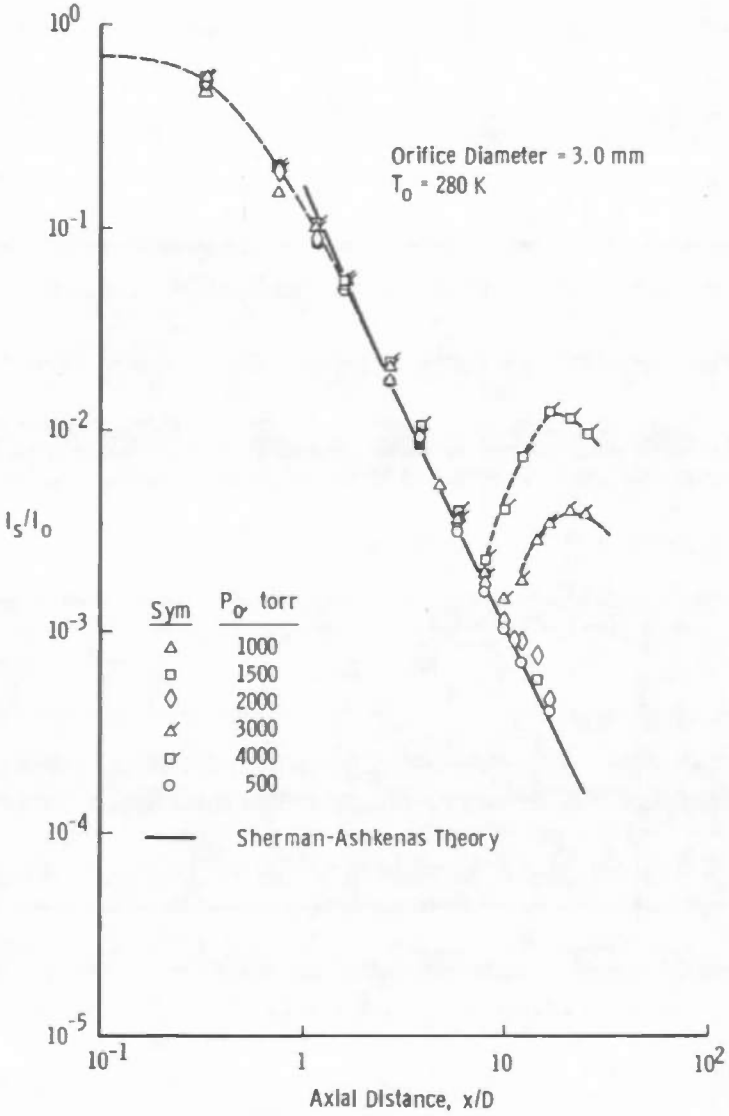

Figure 23. Axial variation of N_2 Rayleigh scattering measurements.

Also shown in Fig. 23, by dashed line, are the results obtained for the isentropic expansion density ratio in the region $x/D < 1$ for which the Ashkenas-Sherman equations are invalid. Reference 15 presents static pressure and Mach number data for the transonic region of the N_2 expansion from a sonic orifice source. Those data show that the Mach number at $x/D = 0$ is approximately equal to 0.70. Using this value of M and isentropic flow relations, one finds the number density ratio predicted at the orifice to be 0.792, and this value is consistent with the extrapolated data of Fig. 23. It is also noted from Fig. 23 that the isentropic density ratio of 0.634 corresponding to a Mach number of one is attained at $x/D = 0.25$, and it is concluded that the axial sonic point of the orifice is located at $x/D = 0.25$. Therefore, continued expansion from $x/D = 0.25$ to $x/D = 1.0$, according to Ref. 15, is required for development of a self-similar flow field with an apparent source located at $x/D = 0.40$.

Figure 24 shows the expansion adiabats plotted in the P-T plane along with the N_2 vapor pressure curve, which was obtained from Ref. 17.

Using the results shown in Figs. 17 through 22, the value of $(x/D)_\theta$ was determined at which condensation onset was just detectable. These values are shown in Fig. 25. Also shown in Fig. 24 are the x/D locations determined from Figs. 17 through 22, for which the value of I_s/I_o exceeded by approximately 10 percent the isentropic, uncondensed value. It is seen from Fig. 25 that as the value of P_o is decreased the onset location moves away from the saturation location to positions farther downstream, indicating higher values of the supersaturation ratio $s = P_s/P_\theta$.

Figure 26 shows the variation of s with P_o for the two previously mentioned limits of condensation. The magnitude of the estimated degrees of supercooling, $T_\theta - T_s$, can be obtained from Fig. 25 and the isentropic curve of Fig. 9. For the 3-mm-diam orifice, it is found that $T_\theta - T_s = 45$ to 50 K for $P_o \lesssim 500$ torr, $T_\theta - T_s = 20$ K for $1000 \lesssim P_o \lesssim 3000$ torr, and $T_\theta - T_s \simeq 0$ K for $P_o > 3000$ torr. Finally, it is noted that the spatial gradient of temperature at onset for the higher values of P_o is approximately 37 K/cm or, in terms of the time rate of change, $dT/dt \approx 2.6 \times 10^6$ K/sec.

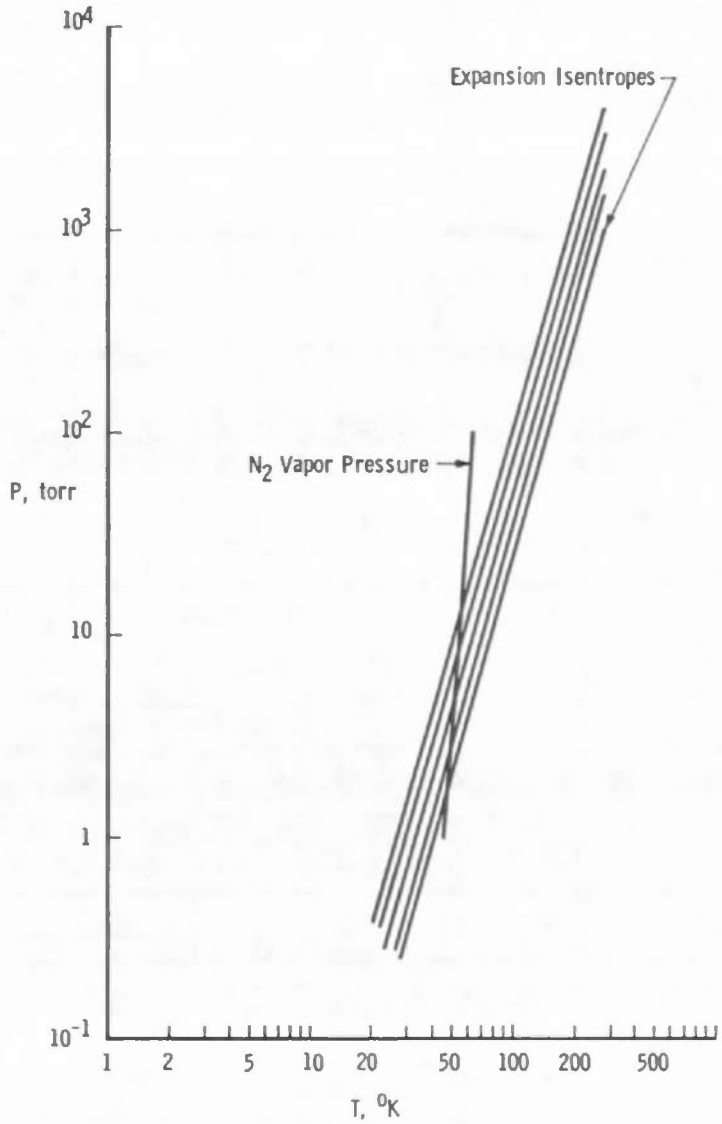

Figure 24. N_2 P-T diagram.

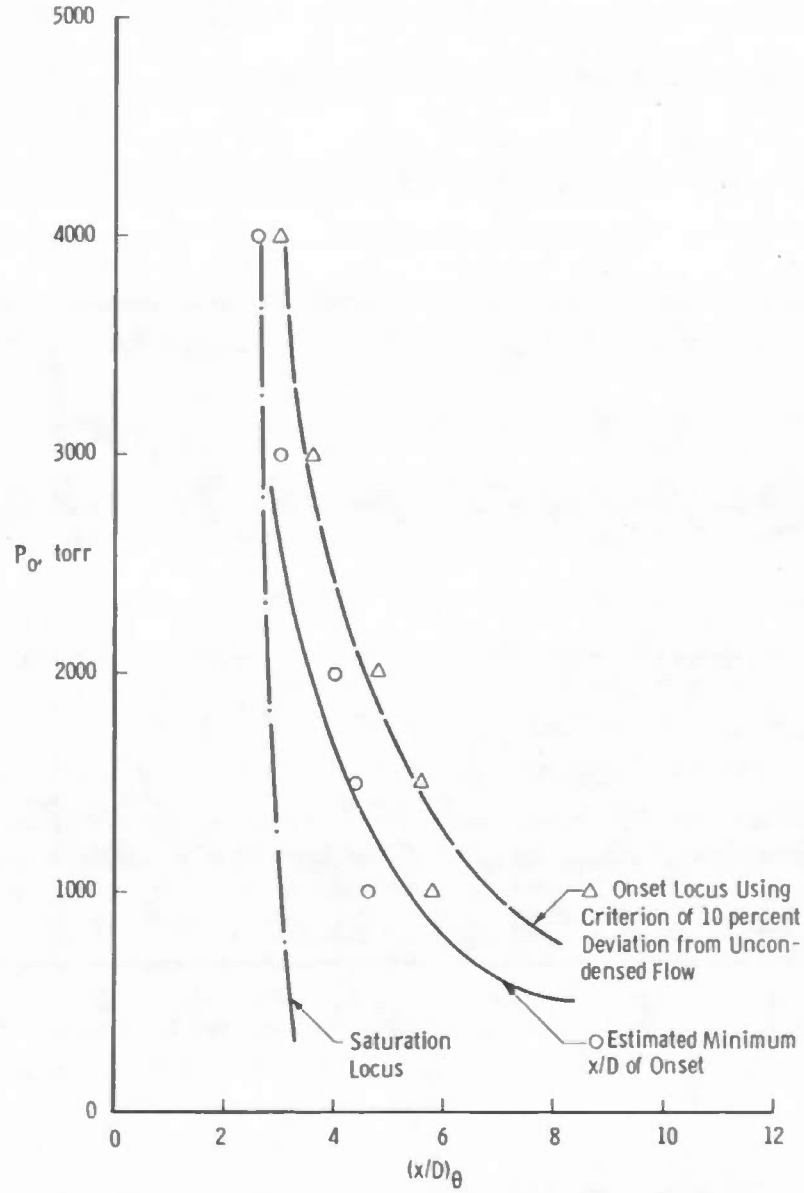

Figure 25. Variation of onset location versus reservoir pressure.

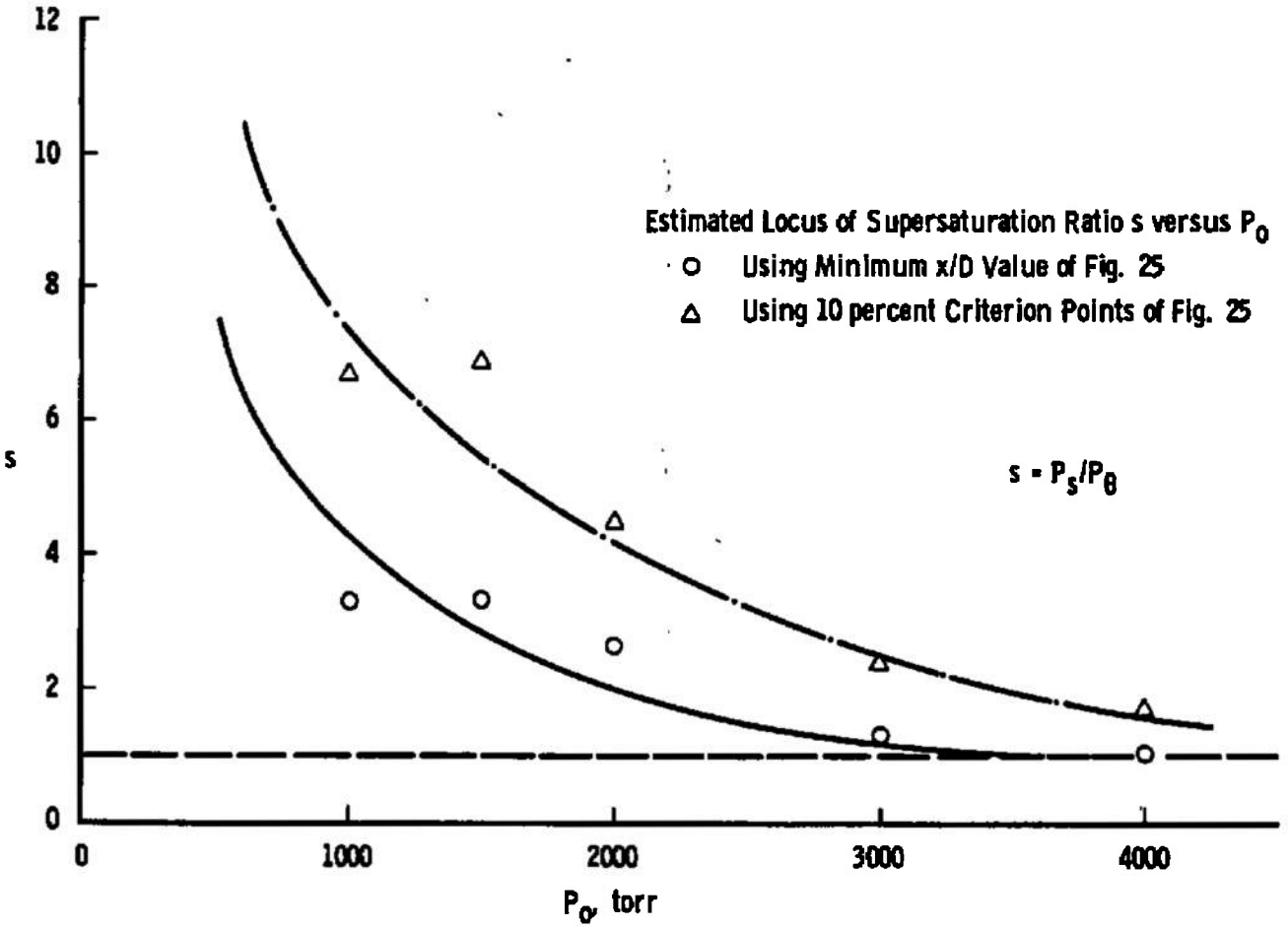

Figure 26. Variation of supersaturation ratios with reservoir pressure.

3.3 ANALYSIS AND DISCUSSION

Considering the Rayleigh scattering results, it is recalled that condensation onset was not observed for P_o = 500 torr, but deviations from the predicted axial dependence of I_s/I_o were seen at 1000 torr. Using the mass spectrometric results of Ref. 3 and using P_o^2D scaling for condensation onset, as indicated by the dimer peak, it is estimated that only dimers exist in the flow field for P_o = 1000 torr, D = 3mm. Therefore, using Eq. (9) the axial variation of the dimer mole fraction for this case was determined. Figure 18 shows the result. Because of the very low signal levels, little weight has been given to the point at x/D = 9.6. Additional justification for this is given by comparisons of

I_s/I_o for P_o = 1500 and 2000 torr where it is seen that the 1000-torr point at x/D = 9.6 is abnormally high. A similar calculation for X_2 for P_o = 1500 torr is shown in Fig. 19, but it is cautioned that these results represent a maximum for X_2 since it is most likely, using mass spectrometric results (Ref. 3), that larger polymers coexist in the flow field. Figures 21 and 22 show the axial variation of the condensate scattering signal, and it is believed that this is indicative of massive condensation. From Fig. 23 the condensate growth and its cessation or freezing point is clearly indicated for P_o = 3000 and 4000 torr.

The axial variations of the T_R/T_o data were analyzed for the purpose of obtaining estimates of the condensate mass fraction. As has been discussed by Sherman (Ref. 18), the enthalpy equation for a one-dimensional condensing flow field can be written as

$$c_p T_o + g \times L = c_p T_c - u_c^2/2 \tag{10}$$

where

g = mass fraction of condensate
L = latent heat of condensate
u_c = flow speed in condensing gas
c_p = specific heat of gas

It has been assumed that g is sufficiently small that the specific heat ratio, γ, remains constant. One finds

$$u_c = \{2[c_p T_o + g \times L - c_p T_c]\}^{1/2} \tag{11}$$

and

$$u = \{2[c_p T_o - c_p T]\}^{1/2} \text{ without condensation} \tag{12}$$

and $u_c/u > 1$ if $gL/c_p T_o > (T_c/T_o) - (T/T_o)$.

That is, augmentation of flow speed can result by condensation. As $x/D \rightarrow \infty$, $(T_c/T_o) \rightarrow (T/T_o) \rightarrow 0$ and $u_c \rightarrow (1 + gL/h_o)^{1/2}$, where h_o is the specific energy of the reservoir.

For small changes in u the ratio of Eqs. (11) and (12) gives

$$(T_R/T_o) - (T/T_o) \approx g \times L/h_o - 2\,\Delta u/u \tag{13}$$

where $\Delta u = u_c - u$ and Δu can be either greater or less than zero, and the temperature of the condensed flow is assumed to be given by the measured value of T_R. To estimate g from the T_R data, it is assumed that the condensation process occurs instantaneously at $(x/D)_\theta$ and the area change of the plume across the assumed infinitesimally small condensation zone is zero. One can then use the well-known, constant area, diabatic flow equations (Ref. 19) to relate parameters across the condensation zone. For diabatic flow with constant area, it is known that heat addition drives the Mach number, M, toward unity for both subsonic and supersonic flow. Therefore, for $M > 1$ at onset, the flow speed, according to this model, initially decreases, and, following a re-expansion of the flow, the flow speed increases and can exceed the isentropic, uncondensed flow speed. To calculate $\Delta u/u$ and g, the T_R/T_o data were extrapolated toward the onset location $(x/D)_\theta$, as indicated by the Rayleigh scattering results, and Fig. 27 shows this extrapolation. The difference between the extrapolated and isentropic curves does not exceed the experimental uncertainty in the T_R/T_o data until x/D equals approximately 5, which was assumed to represent the location of condensation onset as manifested by the increased value of T_R. At this point, it was assumed that onset was instantaneous and of constant area. To calculate the values of $\Delta u/u$ and g, the following procedure was used.

The following constant area diabatic flow equation relating the temperature and Mach number, T and M, respectively, before condensation to their values following condensation, T_c and M_c, was used:

$$T_c/T = f(M_c)/f(M) \tag{14}$$

where

$$f(M) = M^2/(1 + \gamma M^2)^2 \tag{15}$$

and both T and M are assumed to be given by the isentropic equations of Ref. 15 at $(x/D)_\theta$. The degree of condensation is assumed to be sufficiently small that γ is unchanged. The measured, or extrapolated, value of T_R at $(x/D)_\theta$ is assumed to accurately approximate T_c. Equation (14) was used to graphically determine the Mach number M_c, and using the measured value of T_R, the flow speed following condensation,

u_c, was determined. Therefore u_c, coupled with the flow speed value u preceding onset, as determined by the isentropic values of M and T, determines the value of $\Delta u/u$ and, thereby, g, using Eq. (13). Additional diabatic flow equations as given in Ref. 19 were used to graphically determine the values of gas pressure and density following condensation. The following set of values of these aforementioned parameters were calculated according to this procedure:

	Before Condensation	After Condensation	Final-to-Initial Value Ratio
M	6.30	6.0	0.952
T, K	33.6	36.9	1.099
N/N_o	4.30×10^{-3}	4.29×10^{-3}	0.997
u, cm/sec	1.182×10^4	1.179×10^4	0.998
P, torr	0.465	0.510	1.096

The mass fraction of condensate was found using these values to be approximately 1.4×10^{-2}. The value of X_2 from the results of Fig. 18 is approximately 1.7×10^{-2} or a mass fraction of approximately 3×10^{-2}. The agreement between these two independent determinations of g is within approximately a factor of two which is perhaps the best to be expected considering the simple model and extrapolation employed.

Since

$$\lim_{x/D \to \infty} u_c = (1 - gL/h_o)^{1/2}$$

and such velocity augmentation has been reported by Bailey (Ref. 20), it is worth noting that for $g \simeq 1.4 \times 10^{-2}$, the magnitude of Δu of N_2, which may exhibit rotational relaxation effects, is marginal for accurate detection by time-of-flight systems.

It has been noted that the P_o^2D scaled results of Ref. 3 would indicate a predominance of dimers, and this was the primary basis for proceeding with the previous analysis. The data of Yealland et al. (Ref. 4) also support this assumption. Their mass spectrometric results for condensing flow fields of N_2 were fitted to a functional form relating the percentage of dimers in the far field to the reservoir conditions. Using P_o^2D scaling and the equation of Ref. 4, it was found that Yealland et al. predict 0.08, 0.56, and 1.92 percent dimers for P_o = 500, 1000, and 1500 torr, respectively, for a 3-mm orifice. The

uncertainty of the results of Ref. 4 is stated to be approximately a factor of 2, and these results are in order of magnitude agreement with the present results.

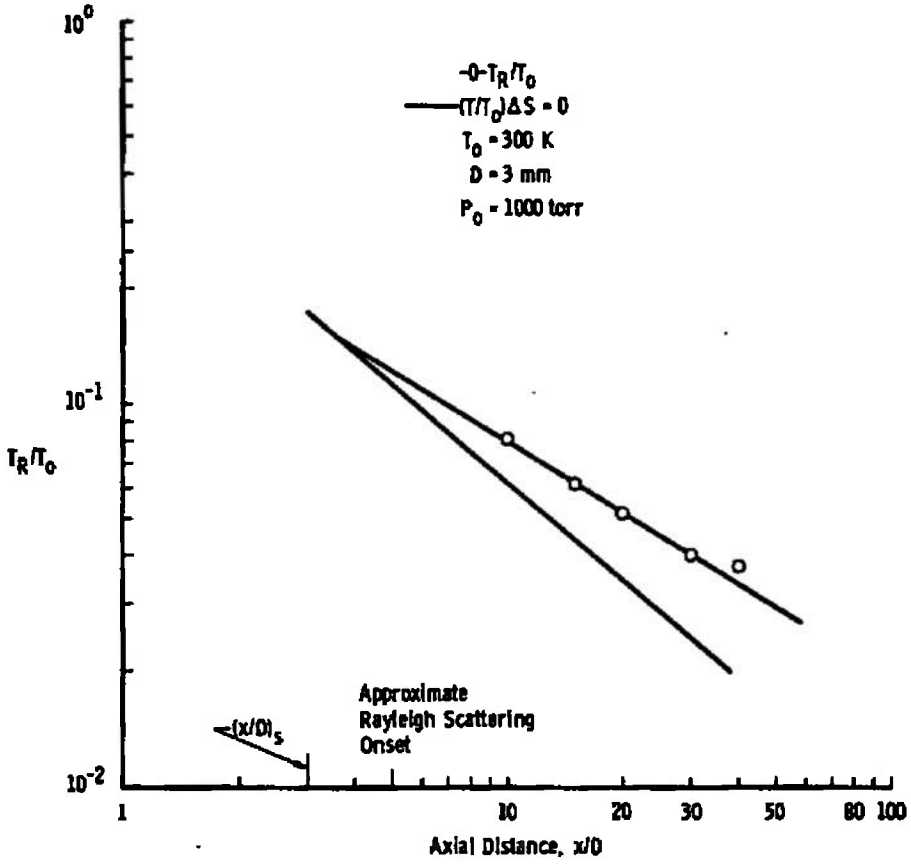

Figure 27. Axial extrapolation of T_R/T_o for diabatic flow analysis.

A similar analysis of the electron beam data for the cases of T_o = 116 K and 133 K was performed. The T_R/T_o data were extrapolated to the saturation point $(x/D)_s$ which was assumed to be the onset location for these temperatures. The mass fraction of condensate was found to be on the order of 4.0×10^{-2} and 1.0×10^{-2} for T_o = 116 K and 133 K, respectively. However, the data scatter and the slight curvature of the T_o = 133 K data extrapolation give greater reliability to the lower temperature expansion.

Concerning the possibility of gross changes in jet characteristics of condensing flow fields, a comparison of the radial profiles of Fig. 11 and Figs. 15 and 16 show that essentially identical radial profiles, nondimensionalized by the axial value, are obtained. However, changes in the value of the absolute temperature were dramatic for flow fields

with condensate mass fraction exceeding approximately one percent, and changes in T were detected even for flow fields containing condensate in the form of only dimers. Insofar as previous mass spectrometric results are concerned, these results aid somewhat in quantifying these previously qualitative results.

It should be noted that the degree of supersaturation predicted by Fig. 1 of Ref. 1 for N_2 flows is greater than that actually found in this work, indicating both an increase in sensitivity for the detection of condensation onset as well as the use of a different criterion.

4.0 CONCLUSIONS

The use of both the electron beam and Rayleigh scattering techniques has provided independent estimates of not only the spatial location of condensation onset but also estimates of the mass fraction of the condensate for a sonic orifice expansion of N_2. The mass fraction of condensate results are in, at best, order-of-magnitude agreement with estimates of previous mass spectrometric results, but it should be noted that orifice diameter and pressure scaling laws were used in regimes not observed by the far-field mass spectrometer investigations. Additional measurements of sonic orifice expansions produced by large orifices, i.e., millimeter size and greater, are required to verify the far-field scaling laws and to observe and correlate the axial growth variation of condensate. More detailed information concerning the gas temperature is required near and at condensation onset, and measurements in progress are utilizing rotational Raman scattering for this purpose.

It should be noted that the degree of supersaturation attainable for the high-purity N_2 flow fields studied was found to be significantly less than that predicted by Ref. 1, and it is suggested that the recommendations of Ref. 1 be used with caution in the design of uncondensed N_2 hypersonic flow facilities.

REFERENCES

1. Daum, Fred L. and Gyarmathy, George. "Condensation of Air and Nitrogen in Hypersonic Wind Tunnels." AIAA Journal, Vol. 6, No. 3, March 1968, pp. 458-465.

2. Wegener, Peter P. Nonequilibrium Gas Flows. Edited by P. P. Wegener, Part I, Marcel Decker, New York, 1969.

3. Golomb, D., Good, R. E., Bailey, A. B., Busby, M. R., and Dawbarn, R. "Dimers, Clusters, and Condensation in Free Jets. II." The Journal of Chemical Physics, Vol. 57, No. 9 November 1972, pp. 3844-3852.

4. Yealland, R. M., Deckers, J. M., Scott, I. D., and Touri, C. T. "Dimer Concentrations in Supersonic Free Jets." Canadian Journal of Physics, Vol. 50, October 1972, pp. 2464-2470.

5. Hagena, O. F. and Obert, W. "Cluster Formation in Expanding Supersonic Jets; Effect of Pressure, Temperature, Nozzle Size, and Test Gas." The Journal of Chemical Physics, Vol. 56, No. 5, March 1972, p. 1793.

6. Beylich, Alfred E. "Condensation in Carbon Dioxide Jet Plumes." AIAA Journal, Vol. 8, No. 5, May 1970, pp. 965-967.

7. Beylich Alfred E. "Experimental Investigation of Carbon Dioxide Jet Plumes." The Physics of Fluids, Vol. 14, No. 5, May 1971, pp. 898-905.

8. Limbaugh, C. C., Lewis, J. W. L., Kinslow, M., Powell, H. M., Price, L. L., and Williams, W. D. "Condensation of Nitrogen in a Hypersonic Nozzle Flow Field." AEDC-TR-74-31 (AD919337L), May 1974.

9. Williams, W. D. and Lewis, J. W. L. "Raman and Rayleigh Scattering Diagnostics of a Two-Phase Hypersonic N_2 Flow Field." AIAA- (to be published).

10. Muntz, E. P. and Marsden, D. J. "Electron Excitation Applied to the Experimental Investigation of Rarefied Gas Flows." Rarefied Gas Dynamics Symposium, Vol. II, Edited by J. A. Laurmann, Academic Press, Inc., New York, 1963, pp. 495-526.

11. Williams, W. D., Hornkohl, J. O., and Lewis, J. W. L. "Electron Beam Probe for a Low Density Hypersonic Tunnel." AEDC-TR-71-61 (AD727004), July 1971.

12. Marrone, Paul V. "Rotational Temperature and Density Measurements in Underexpanded Jets and Shock Waves Using an Electron Beam Probe." University of Toronto Institute for Aerospace Studies Report No. 113, April 1966.

13. Hirschfelder, J. O., Curtis, C. F., and Bird, R. B. Molecular Theory of Gases and Liquids. John Wiley and Sons, New York, 1954.

14. Kerker, Milton. The Scattering of Light, and Other Electromagnetic Radiation. Academic Press, New York, 1969.

15. Ashkenas, H. and Sherman, F. S. "The Structure and Utilization of Supersonic Free Jets in Low Density Wind Tunnels." Rarefied Gas Dynamics. Edited by J. H. de Leeuw, Fourth Symposium, Vol. II, Academic Press, New York, 1966, pp. 84-105.

16. Williams, William D. "Laboratory Verification Studies of Rotational and Vibrational Temperature Measurements by the Electron Beam Technique." AEDC-TR-68-265 (AD683001), February 1969.

17. Hilsenrath, J., Beckett, C. W., Benedict, W. S., Fano, L., Hoge, H. J., Masi, J. F., Nuttall, R. L., Touloukian, Y. S. and Woolley, H. W. Tables of Thermal Properties of Gases. NBS Circular 564, Washington, D. C., November 1955.

18. Sherman, P. M. "Condensation Augmented Velocity of a Supersonic Stream." AIAA Journal, Vol. 9, No. 8, August 1971, pp. 1628-1630.

19. Cambel, Ali Bulent and Jennings, Burgess H. Gas Dynamics. McGraw-Hill, 1958.

20. Bailey, A. B. "Effects of Condensation on Gas Velocity in a Free-Jet Expansion." AEDC-TR-73-93 (AD762503), June 1973.

NOMENCLATURE

a	Particle radius
c_p	Specific heat at constant pressure
D	Orifice diameter
g	Condensate mass fraction
I_o	Incident laser beam intensity
I_s	Scattered laser beam intensity

K_a	Optical calibration constant for Eq. (3)
K_α	Optical calibration constant for Eq. (1)
L	Latent heat of sublimation
M	Mach number
m	Index of refraction
N	Number density
N_i	Number density of i-mer
N/Z	Number-to-charge ratio for cluster
P	Pressure
P_B	Background pressure
S	Entropy
s	Supersaturation ratio
T	Temperature
T_R	Rotational temperature
u	Flow speed
X_i	Mole fraction of i-mer
x	Axial distance
y	Radial distance
α, $\bar{\alpha}$	Scalar and tensor molecular polarizability, respectively
α_i	Polarizability of i-mer
ΔS	Change in entropy
Δu	Change in u caused by condensation
γ	Specific heat ratio
λ	Wavelength

SUBSCRIPTS

c	Variable evaluated for condensing flow
o	Reservoir value

s	Saturation value
T	Total
θ	Condensation onset value

CGS units used unless stated otherwise.